

1      **Discovery of a new evolutionarily conserved short linear F-actin binding motif**

2      Themistoklis Paraschiakos<sup>1\*</sup>, Biao Yuan<sup>2,5, 6, 3\*</sup>, Kostiantyn Sopelniak<sup>4</sup>, Michael Hecht-Bucher<sup>1</sup>,  
3      Lisa Simon<sup>1</sup>, Ksenija Zonjic<sup>1</sup>, Dominic Eggers<sup>1</sup>, Franziska Selle<sup>1</sup>, Jing Li<sup>1</sup>, Stefan Linder<sup>4</sup>,  
4      Thomas C. Marlovits<sup>2, 5, 6</sup>, and Sabine Windhorst<sup>1</sup>

5

6

7

8      <sup>1</sup>Department of Biochemistry and Signal Transduction, University Medical Center Hamburg-  
9      Eppendorf, Martinistraße 52, D-20246 Hamburg

10     <sup>2</sup> Institute of Microbial and Molecular Sciences, University Medical Center Hamburg-  
11    Eppendorf, Notkestrasse 85, D-22607 Hamburg

12     <sup>4</sup> Institute for Microbiology, Virology and Hygiene, University Medical Center Hamburg-  
13    Eppendorf, Martinistraße 52, D-20246 Hamburg<sup>4</sup>

14     <sup>5</sup> CSSB-Center for Structural Systems Biology, Notkestrasse 85, D-22607 Hamburg

15     <sup>6</sup> Deutsches Elektronen Synchrotron (DESY), Notkestrasse 85, D-22607 Hamburg

16

17     <sup>3</sup> current address: Molecular Structural Biology, Helmholtz Center for Infection Research,  
18    Inhoffenstraße 7, 38124, Braunschweig

19

20     \*These authors contributed equally to this work

21

22      **Address correspondence to:**

23      Sabine Windhorst

24      Department of Biochemistry and Signal Transduction,

25      University Medical Center Hamburg-Eppendorf,

26      Martinistraße 52,

27      D-20246 Hamburg

28      Germany

29      Tel. +49-40-7410-56013

30      E-Mail: [s.windhorst@uke.de](mailto:s.windhorst@uke.de)

31

32

33    **Abstract**

34    Regulation of the actin cytoskeleton by actin binding proteins (ABPs) is essential for cellular  
35    homeostasis, and the mode of actin binding determines the activity of ABPs. Here, we  
36    discovered a novel “Short linear F-actin binding motif (SFM)” on the basis of the cryo-EM  
37    structure of the ITPKA-F-actin complex. We developed the computational pipeline SLiMFold,  
38    which identified 103 human SFM containing-proteins exhibiting diverse cellular functions. The  
39    SFM probably developed *ex nihilo* and remained conserved in eukaryotes, with a binding  
40    affinity to F-actin ranging from 13 to 89 μM. Furthermore, we uncovered the essential amino  
41    acids of this SFM for F-actin binding and affinity modulation. Together, the SFM seems to serve  
42    as a low affinity anchor to target proteins to F-actin, in order to connect the regulation of actin  
43    dynamics with broad cellular functions. These findings will shed new light on the role of a wide  
44    variety of proteins.

45

46 **Introduction**

47 Actin filaments (F-actin) form a dynamic cytoskeletal framework in eukaryotic cells, driving  
48 essential processes such as cell motility, division, and morphogenesis. These processes are  
49 orchestrated by different interacting proteins, referred to as actin-binding proteins (ABPs),  
50 along with signalling and scaffolding proteins.<sup>1</sup> These proteins assist in polymerisation,  
51 nucleation, elongation or capping, severing, crosslinking, or bundling of actin filaments, and  
52 are required to coordinate spatially restricted actin turnover. Their impact on actin dynamics  
53 depends on the affinity of the actin-binding domain (ABD) and, in most cases, on cellular  
54 stimulation<sup>2</sup>. Many ABPs are inhibited in resting cells, and a lot of them are activated by small  
55 GTPases, RhoA, Cdc42, or Rac<sup>3</sup>. Failures in the regulation or expression of ABPs as well as  
56 mutations can lead to severe diseases, such as neuronal and immunological disorders and  
57 cancer<sup>4–8</sup>.

58 Among the ABPs, a lot of conserved domains and motifs have been identified, upon which  
59 ABP-families with similar functions were defined. Supplementary Table 1 illustrates how the  
60 remarkable variety of motifs and domains matches the diversity of cellular actin functions.  
61 Despite this diversity, a lot of ABPs bind to a hydrophobic cleft between actin subdomain 1 and  
62 3, such as cofilin-1, T-plastin, myosin and gelsolin<sup>9</sup>. Here, the binding modus and/or the affinity  
63 is different, resulting in competition of the ABPs to each other in response to cellular stimulation  
64 or under certain pathological conditions<sup>10,11</sup>.

65 Alongside globular domains with properly folded three-dimensional structure, such as that of  
66 cofilin-1, T-plastin, myosin and gelsolin, unstructured regions have been shown to play an  
67 essential role in many dynamic cellular processes<sup>12–21</sup>. Among these, the most common  
68 functional modules are short amino acid stretches known as short linear motifs (SLiMs)<sup>22–25</sup>.  
69 The abundant G-actin binding WH2 (Wiskott-Aldrich homology 2) motif is a prominent example  
70 of a SLIM, and structure elucidation revealed that it binds to G-actin at the hydrophobic cleft  
71 between actin subdomains 1 and 3, thereby modulating polymerisation and filament  
72 dynamics<sup>26</sup>. Missense mutations located inside the WH2 motif are associated with diseases,

73 i.e. the human Leiomodin-3 (Lmod3), where mutations R543L<sup>27</sup> or L550F<sup>28</sup> are associated  
74 with Nemaline myopathy 10 (NEM10). Moreover, WH2 motifs can also be part of bacterial  
75 effector proteins, often leading to restructuring of the host cell actin cytoskeleton and promoting  
76 either efficient colonisation (VopL/VopF) or bacterial motility during infection (Sca2 and  
77 RickA)<sup>29–32</sup>.

78 In this study, we identify a novel short linear F-actin binding motif (SFM) that mediates F-actin  
79 binding in diverse human proteins with low affinity. Comparative sequence analyses indicate  
80 that the SFM is under purifying selection and acts as a low-affinity anchor, targeting various  
81 cytosolic proteins to the actin cytoskeleton. Notably, our findings not only unify previously  
82 observed yet unclassified sequences under this defined motif, but also enable the prediction  
83 of new SFM-containing proteins. These observations point to a broader role for the SFM in  
84 cytoskeletal organization under both physiological and pathophysiological conditions and may  
85 uncover new cellular actin networks and mechanisms.

86

## 87 **Results**

88

### 89 **Structural insight into ITPKA in F-actin binding**

90 A high number of actin-binding proteins (ABPs) contain uncharacterized domains responsible  
91 for F-actin binding, including the human Inositol-trisphosphate 3-kinase A (ITPKA)<sup>10,33–36</sup>. This  
92 InsP<sub>3</sub>Kinase isoform constitutively binds to F-actin, and due to homodimer formation it exhibits  
93 F-actin bundling activity<sup>36</sup>. Under physiological conditions, ITPKA contributes to control the  
94 postsynaptic actin architecture of hippocampal neurons. However, ITPKA is also expressed in  
95 different malignant tumor cells, and its actin bundling activity induces the formation of cellular  
96 protrusions essential for invasion of cancer cells<sup>34,37</sup>.

97 To investigate the molecular basis of ITPKA for F-actin binding in detail, we solved the cryo-  
98 EM structure of the ITPKA-F-Actin complex at 2.97 Å resolution. In this structure, the F-actin  
99 binding domain (ABD) of ITPKA is clearly visible, whereas the catalytic domain and the linker

100 connecting it to the ABD were not resolved (Figure 1a, and Extended Data Figure 1),  
101 confirming that the C-terminal InsP<sub>3</sub>Kinase domain is not directly involved in F-actin binding.  
102 The amino acids Arg28 to Ala49 bind to the hydrophobic cleft between actin subdomains 1 and  
103 3, and also contacts the DNase-binding loop of the adjacent actin subunit (A<sub>-2</sub>) (Figure 1a, and  
104 Extended Data Figure 1). In parallel to us, the Belyy group resolved the cryo-EM structure of  
105 F-actin bound by F-tractin, which represents the core actin binding domain of ITPKA and is  
106 used as F-actin marker for live cell imaging<sup>11,38</sup>. This structure matches our findings of the F-  
107 actin binding mode<sup>11</sup>.

108 Collectively, we found that the core actin binding domain of ITPKA only comprises 21 amino  
109 acids folded into an alpha helix. Interestingly, this peptide exhibits the characteristics of a short  
110 linear motif (SLiM), and its structure resembles that of the F-actin probe Lifeact<sup>11,39,40</sup>. Based  
111 on this consideration, we performed a structural alignment of ITPKA<sup>Arg28-Ala49</sup> with Lifeact (PDB:  
112 7BTE and 7AD9) and found highly similar helix positioning, including the aligned positions Val  
113 (P1), Leu (P4), Phe (P8), and Glu (P9) (Figure 1b,c, d).

114 This discovery let us to propose the F-actin binding SLiM VxxLxxxFE, and to determine  
115 whether other human proteins include this motif, we developed a computational pipeline, called  
116 SLiMFold (Figure 1e). First, we derived a Position Specific Scoring Matrix (PSSM) from the  
117 aligned sequences of ITPKA<sup>Arg28-Ala49</sup>—and Lifeact (see Figure 1e and Extended Data Figure 2),  
118 and used it to screen against the NCBI human protein database. Next to this PSSM cutoff, we  
119 applied PSIPRED<sup>41</sup>, ANCHOR<sup>42</sup>, and IUPred<sup>43</sup> cutoffs to highlight candidates containing this  
120 SLiM (Figure 1e upper panel). For each of these 539 hits a multiple sequence alignment (MSA)  
121 was performed via jackhmmer<sup>44</sup> against UniRef90 database, with optimized parameters to  
122 improve both speed and coverage.

123 Once the MSAs were compiled, we ran a custom ColabFold notebook to predict the structure  
124 of various peptide–actin complexes, leveraging the user-provided MSAs instead of  
125 recalculating new ones. Each peptide–actin model was scored by pLDDT, pTM, and ipTM, and

126 any candidate with mean ipTM below 0.6 (averaged over the top three ranked models) was  
127 excluded (Figure 1e lower panel, and Figure 1f).

128 To assess structural convergence with the reference ITPKA<sup>Arg28-Ala49</sup> motif, each candidate  
129 underwent a detailed comparison against the ITPKA<sup>Arg28-Ala49</sup>-actin complex. We measured  
130 RMSD for  $\alpha$ -carbon atoms (positions P1–P9), helix orientation ( $\Delta\theta$ ,  $\Delta\phi$ ) using a polar  
131 coordinate system, and helix polarity (Figure 1f, g, h). The resulting models were then clustered  
132 using HDBSCAN<sup>45</sup>, which effectively segregates core clusters from outliers (Figure 1i).  
133 Cluster 3—enriched in 59 gene sequences—displayed minimal RMSD and orientation shifts  
134 relative to ITPKA, suggesting a highly similar helix arrangement for actin binding (Figure 1i). A  
135 sequence logo of these 59 clustered hits confirmed strong positional conservation at P1, P4,  
136 P8, and P9, with P1 and P8 showing the highest degree of conservation (Figure 1j). Since this  
137 actin binding motif belongs to the SLiMs, it was designated as Short linear F-actin binding Motif  
138 (SFM).

139

#### 140 **Validation of SFM-peptides *in cellulo* and *in vitro***

141 To validate binding of the predicted SFM-peptides to F-actin, we randomly selected  
142 candidates, and split them into two groups. Group 1 included the RhoGTPase-guanine  
143 exchange factors (GEFs) FGD1, FGD4, DENNDC1, and ARHGEF11, as well as DIXDC1, a  
144 protein that is involved in regulation of wnt-signalling (Figure 2a). Group 2 comprised the actin  
145 bundling proteins SHROOM 3, ESPNL, and PPP1R9A, the ubiquitin specific protease USP54,  
146 the z-disc protein CEFIP and the tight junction protein CGNL1 (Figure 3a). Group 1 candidates  
147 were validated by F-actin-colocalization with EGFP-peptides or full-length proteins in primary  
148 human macrophages as well as in H1299 lung cancer cells, and Group 2 candidates were  
149 validated by F-actin co-sedimentation assays with recombinant peptides.

150 The Group 1 SFM peptides, including the positive controls ITPKA<sup>Arg28-Ala49</sup> and Lifeact, were  
151 transiently expressed as EGFP-fusion peptides in primary human macrophages, allowing a

152 precise quantification of co-localization with F-actin subsets<sup>46</sup>. We additionally tested site-  
153 specific mutants (V→A and F→A) at positions 1 and 8. As shown in Figure 2 (and Extended  
154 Data Figure 4), Lifeact, ITPKA<sup>Arg28-Ala49</sup>, FGD4 and ARHGEF11 showed prominent co-  
155 localization with podosome cores. However, DENND1C mainly localized to the podosome cap,  
156 and also FGD1 showed a broader distribution, encompassing parts of the podosome core. On  
157 the other hand, all P1/P8 mutants were diffusely distributed, confirming that positions P1 and  
158 P8 inside the SFM are essential for F-actin binding. Similar results were obtained also in H1299  
159 lung cancer cells (Extended Data Figure 5). Together, these data indicate that the SFM binds  
160 to F-actin with different efficiency, and preference to F-actin subpopulations.

161 To further confirm these findings, we tested full-length versions of selected proteins in H1299  
162 cells and introduced the mutations at P1/P8 position. Colocalization with F-actin was observed  
163 for the wild-type full-length proteins but completely disappeared upon mutation of the residues  
164 at P1/P8 position (Extended Data Figure 6). This result highlights the critical role of the SFM  
165 in mediating F-actin binding, not only in isolated peptides but also in full-length proteins.

166 For Group 2 candidates affinities of peptides to F-actin were tested. For this purpose, the  
167 peptides were recombinantly expressed as EGFP-fusion peptides in bacteria, and after  
168 purification its binding to F-actin was assessed by a co-sedimentation assay. After employing  
169 different F-actin concentration, dissociation constants ( $K_D$ ) were calculated, showing that the  
170 SFMs of CEFIP and USP54, of ITPKA and PPP1R9A, and of CGNL1 and ESPNL bound with  
171 very similar affinities to F-actin (13 µM, 30 µM, and 50 µM) while the affinity of SHROOM 3  
172 was lowest (90 µM) (Figure 3). These data reveal a relative low F-actin binding affinity of the  
173 SFM-peptide with high variations among the different peptides.

174

175 **Amino acids in between the conserved Valine (P1) and Phenylalanine (P8) determine  
176 affinity of the SFMs**

177 Our data depicted in Figure 3b reveal that although all SFM-peptides tested included the  
178 conserved amino acids at P1/P8 position, their binding affinities to F-actin were different. This  
179 raises the question as to whether amino acids (aa) flanking the motif modulate the affinity.

180 To address this, we aimed to identify the aa inside the SFM mediating the highest affinity to F-  
181 actin. For this purpose, the jackhammer generated MSAs of the peptide sequences from  
182 ITPKA, CEFIP, PPP1R9A, USP54, FGD4, ARHGEF11, DIXDC1, and Lifeact were used to  
183 generate a position-specific frequency matrix (PSFM) (Figure 3c).

184 Aligning homologous sequences from these motifs served as a “contrast enhancer”, revealing  
185 positions that appear intolerant to certain physiochemically similar amino acid groups (white  
186 squares in Figure 4c) or potentially essential for F-actin binding (red squares in Figure 4c). On  
187 the basis of this matrix, three hotspots were defined, an N-terminal, an internal, and a C-  
188 terminal motif. To test whether substitution of low frequency amino acid with high frequency  
189 amino acid would enhance the binding affinity to F-actin, targeted mutations in SHROOM3 and  
190 USP54 were introduced according to these hotspots. In SHROOM3, point substitutions  
191 Y1I/C6S (M2), K11L (M3), and Q17A/E19C/Q23A (M4) were produced, along with a triple-  
192 hotspot variant (M1). Similarly, USP54 mutants F1I/L7S (M2), A12I/Q16E (M3), M18I/M23A  
193 Indeed, after assessing binding of the wt and mutant peptides to F-actin we found that mutation  
194 of the amino acids between the conserved V(P1)/F(P8) positions (internal motif) increased  
195 binding to F-actin four-fold in SHROOM 3 (mutant S2) and three-fold in USP54 (Mutant U2)  
196 compared to wt protein. However, mutations N- or C-terminal to the V(P1)/F(P8) positions  
197 (Mutants S1, S3, U1, U3) had no significant effects (Figure 3e). Moreover, determination of  
198 USP54 M1 (triple-hotspot variant) affinity to F-actin revealed a  $K_D$  of 3.7  $\mu\text{M}$  (Figure 3f),  
199 confirming increased binding of the mutant to F-actin.

200 In summary, our data show that the conserved amino acids at P1 and P8 position are required  
201 for binding of the SFM-motif to F-actin, and reveal that those residues in between modulate  
202 affinity.

203

204 **The amino acids inside the SFM are conserved over evolution**

205 To examine the evolutionary conservation of the SFM motif, we generated sequence logos for  
206 12 validated SFM-containing proteins across *Crocodylia*, *Aves*, *Testudines*, *Lepidosauria*,  
207 *Mammalia*, *Amphibia*, *Coelacanthiformes*, and *Actinopteri*. These seven classes were chosen  
208 because, with the exception of Lifeact (which is found only in *Saccharomyces* and thus not  
209 represented in these classes), they cover all known occurrences of the SFM in our studied  
210 dataset. The resulting logos consistently highlighted Val (P1), Leu (P4), Phe (P8), and Glu (P9)  
211 as predominantly invariant across the examined taxa. Although a small number of substitutions  
212 were observed at these positions in certain species, these core residues remained largely  
213 unchanged, indicating strong evolutionary constraints (Figure 4a). This observation aligns with  
214 our initial comparison of ITPKA and Lifeact (Figure 1), where a similar set of core residues  
215 were conserved. To accurately quantify the selective forces acting on these conserved  
216 positions, we calculated the non-synonymous to synonymous substitution ratio (dN/dS) within  
217 each SFM-containing gene across the taxa in which the motif was confidently detected. We  
218 then averaged these values around the SFM's core (Val (P1) to Glu (P9)) for all proteins. The  
219 resulting low dN/dS ratio (relative to nearby flanking regions) strongly suggests that the SFM  
220 is under purifying (negative) selection, consistent with its implied functional importance  
221 (Figure 4b). Consistent with AlphaMissense pathogenicity scores<sup>47</sup> (Extended Data Figure 8),  
222 this highlights the critical necessity of these amino acids for cell survival.

223 To get further insight into evolutionary development of the motif, phylogenetic trees were  
224 constructed and traced each validated SFM-containing protein back to its most recent common  
225 ancestor (MRCA). This analysis revealed a relative early appearance of SHROOM3 in  
226 *Bilateria*, followed by PPP1R9A, DIXDC1 and CGNL1 in *Vertebrata*. CEFIP and ITPKA  
227 emerged in *Euteleostomi*, and by the time of *Gnathostomata* USP54, FGD1, FGD4, ESPN,  
228 DENND1C were present (Figure 4c). Despite this broad taxonomic distribution, we found no

229 evidence of exon duplication or shuffling that might have repurposed an older motif. These  
230 observations support a convergent evolution and a spontaneous origin (*ex nihilo*) of the SFM.

231 To conclude, phylogenetic analysis confirms the conserved nature of the SFM motif, and  
232 indicates an *ex nihilo* development.

233

234 **Final iteration of the SLiMFold pipeline delivers 103 new SFM-candidates with different  
235 biological roles**

236 Finally, we refined the PSSM of the SLiMFold pipeline by incorporating our newly identified  
237 SFM peptides, then performed two additional iterations to compile a definitive list of putative  
238 human SFM proteins (Figure 5a and Extended Data Figure 9). In total, 124 final SFM  
239 sequences emerged in 103 genes (summarized in Table 1). Of these, 26 proteins—including  
240 both our experimental validations and those reported in the literature<sup>48–68</sup>—have been tested  
241 using truncation-based approaches for the SFM. Additionally, 16 other proteins are known to  
242 bind F-actin through more indirect methods (e.g., colocalization or co-sedimentation of the full-  
243 length protein)<sup>69–85</sup>. Further testing and more detailed truncation studies are still needed to  
244 validate the remaining predicted proteins.

245 In order to get information about the biological role of the new SFM-proteins, Gene Ontology  
246 analysis and manual database research, including Uniprot, NCBI, and PubMed, revealed that  
247 they are involved in the regulation of diverse cellular functions (Figure 5b, Extended Data  
248 Figure 10 and Table 1). The largest group encompassed the proteins that directly bind to and  
249 modulate actin. These include well-described actin modulators, such as Cortactin (CTTN),  
250 Caldesmon (CALD1) and Supervillin (SVIL), and many other less investigated proteins. This  
251 group is followed by actin regulators, mostly belonging to the RhoGTPase activators (GEFs)  
252 or silencers (GAPs). Also, we found microtubule associated proteins, signaling proteins, and  
253 proteins involved in the regulation of chromatin, DNA and RNA. The SFM was also identified  
254 in proteins, involved in adhesion, junction, focal adhesion, and cilia-proteins.

255 In conclusion, the SFM is included in highly diverse proteins which is in accordance with our  
256 finding that the peptides have arisen spontaneously in evolution.

257

258 **Discussion**

259 Actin binding proteins (ABPs) are essential for the control of cellular actin dynamics, and  
260 mutation, mis-expression or deletion of ABPs can induce severe diseases<sup>4-8</sup>. The biological  
261 role of ABPs is defined by their actin binding mode, and its targeting to actin can alter  
262 cytoskeletal dynamics, enzyme activity, or cellular localization (reviewed in <sup>86,87</sup>). In this study,  
263 we present the discovery of a new short linear F-actin binding motif (SFM), and provide first  
264 evidence for its biological role.

265 Detailed mutation analysis revealed that inside the SFM VxxLxxxFE, the valin (P1) and  
266 phenylalanine (P8) are essential to bind to F-actin while the amino acids in between modulate  
267 affinity, thus are important. This finding was confirmed by evolution analysis. Also, a low dN/dS  
268 ratio at these positions evidenced purifying selection and a strong evolutionary drive to retain  
269 functional F-actin-binding capacity.

270 Moreover, phylogenetic analysis indicates that the SFM emerged spontaneously (*ex nihilo*)  
271 rather than via exon shuffling or domain duplication. Most likely the motif randomly developed  
272 from point mutations, and since it provided a new functionality, it was negatively selected. This  
273 *ex nihilo* development seems to be typical for SLiM evolution, among which classical examples  
274 are nuclear import and export motifs as well as the calmodulin binding site<sup>88</sup>. Similar to the  
275 SFM, they target highly diverse proteins to cellular destinations or mediate binding of protein  
276 interaction partners (reviewed in <sup>89</sup>).

277 Accordingly, the SFM-containing proteins can be categorized into eight main groups: (1)  
278 regulation of microtubule, (2) cilia, (3) cell junctions, (4,5) actin, (6) signal transduction (7)  
279 nuclear structure and RNA processing, (8) chromatin regulation and DNA repair. Among these,  
280 the SFM-containing proteins involved in actin regulation encompass the highest number of

281 proteins. These include actin binding proteins known to bind to actin via canonical actin binding  
282 motifs such as CTTN<sup>52,90</sup>, FHOD3, SVIL, MYO18A, MYO15B and CALD1 as well as RhoGEFs  
283 and RhoGAPs whose actin binding activity is partly described.

284 Since the SFM only mediates weak F-actin binding, we assume that it has a synergistic or  
285 additive effect on proteins targeted to actin by canonical actin binding domains. Indeed, for  
286 CTTN (cortactin) it has been shown that in addition to the cortactin repeats an adjacent linker,  
287 which includes the SFM, is required to mediate high affinity binding to F-actin<sup>52</sup>. Since cortactin  
288 stabilizes Arp2/3 F-actin branches, this activity may be important for the maintenance of  
289 cellular protrusions. Also, for CALD1 (Caldesmon) the SFM has been identified, and it has  
290 been shown that its binding to actin could be displaced by calmodulin, indicating that SFM-  
291 mediated actin binding is weakened after cellular stimulation<sup>50</sup>. A synergistic or additive effect  
292 of the SFM on actin binding may also work in actin binding proteins containing SFM repeats,  
293 including XIRP1, XIRP2, PPP1R9B, and SHROOM3. Also, the actin-regulating Rho-GTPase  
294 PLEKHG3 include SFM repeats, and its deletion abrogates cell polarity of 3T3 fibroblasts<sup>61</sup>.  
295 Moreover, depletion of the SFM-based actin-binding site in the RhoGEF ARHGEF11 disrupts  
296 the balance between Rac and Rho signaling, impairing the formation of leading-edge  
297 protrusions and trailing-edge retractions in cancer A431 cells<sup>91</sup>. Likewise, SFM repeats are  
298 present in the signaling proteins, SORBS1, SORBS2, and SSH2.

299 However, ITPKA only includes one SFM, but its deletion had strong effects on the actin  
300 architecture as well as on invasion of lung cancer cells<sup>37</sup>, showing that SFM repeats are not  
301 essentially necessary for actin targeting. Also, ITPKA is a good example for actin binding  
302 proteins involved in the regulation of signal transduction. Deletion of the ITPKA-SFM  
303 significantly reduced the InsP<sub>3</sub>Kinase activity of ITPKA<sup>36</sup>, and thereby alters calcium signaling  
304 in hippocampal neurons and cancer cells<sup>10,34</sup>. Likewise, the cancer-related protein kinase  
305 PEAK is targeted to actin, and phosphorylates the focal adhesion protein paxillin, indicating  
306 that its actin targeting coordinates the architecture of focal adhesions after integrin activation<sup>60</sup>.  
307 In lymphocytes, HCLS1 is a substrate of tyrosine kinases, and activates the Arp2/3 complex

308 after SFM-controlled actin binding<sup>54</sup>. Thus, it seems that SFM-mediated actin targeting  
309 represents a signaling hub integrating actin dynamics and cellular signal transduction.

310 Moreover, for ZO-1 (TJP1) it could be shown that deletion of its SFM alters the barrier function  
311 in kidney MDCK cells, indicating that the SFM exhibits an important function in connecting the  
312 actin cytoskeleton with cellular junctions<sup>67</sup>. However, currently there are no studies analyzing  
313 actin targeting of SFM-proteins involved in the regulation of cilia, microtubule, chromatin  
314 modification, DNA repair, nuclear structure and RNA processing. These groups encompass  
315 proteins with broad cellular function such as the kinesins KIF21B and KIF23, as well as the  
316 DNA demethylating TET3, and it will be very exciting to elucidate their role in actin targeting in  
317 future studies. Finally, two main questions should be addressed in future studies: (1) Does the  
318 SFM provide a broad cellular network, or (2) does it define local molecular circuits refined  
319 during evolution to adapt to environmental changes? Since the SFM may have developed *ex*  
320 *nihilo*, the second hypothesis is more likely. However, future studies are necessary to prove  
321 this assumption.

322 In conclusion, SFM-mediated F-actin targeting regulates the properties of diverse cellular  
323 proteins, and we strongly assume that future studies will uncover yet not identified biological  
324 roles. Moreover, expanding our motif search to include non-human databases could reveal the  
325 conservation and functional diversity of SFMs across different species, providing deeper  
326 evolutionary insights and potentially identifying novel SFM-containing proteins. Looking  
327 forward, we envision that the elucidation of the biological role of SFM-proteins will uncover yet  
328 unknown cellular regulation mechanisms involved in physiological and pathological settings.

329

330

331

332 **Methods**

333 **Pipeline Overview**

334 The identification of F-actin-binding SLiMs was performed using the SLiMFold pipeline, which  
335 integrates multiple bioinformatic tools to systematically identify, filter, and validate candidate  
336 motifs. The pipeline was executed in three sequential iterations, refining results at each step  
337 to improve specificity and accuracy.

338 **1. Prerun**

339 The process begins with **Prerun.ipynb**, where hypothesized SLiMs (in this work, the aligned  
340 sequences of ITPKA and Lifeact ABDs from P1 to P9) were used along with the BLOSUM62  
341 substitution matrix<sup>92</sup> to create a position-specific scoring matrix (PSSM). This PSSM was used  
342 to scan the human proteome (NCBI Taxonomy ID: 9606) for putative motif hits. To further filter  
343 out false positives, we incorporated the following criteria:

- 344 • **PSSM Score:** The matrix was used to score sequences in the database, identifying  
345 motifs similar to the hypothesized SLiMs<sup>93</sup>.
- 346 • **IUPRED:** Predicts intrinsically disordered regions, highlighting regions suitable for motif  
347 embedding. The mean IUPRED score was calculated for the motif and its 60-residue  
348 flanking regions (N- and C-terminal)<sup>43</sup>.
- 349 • **ANCHOR:** Identifies regions in intrinsically disordered regions likely to bind structured  
350 partners. The mean ANCHOR value was calculated within the motif<sup>42</sup>.
- 351 • **PSIPRED:** Predicts the probability of secondary structures (helix, beta strand, and  
352 random coil)<sup>41</sup>.

353 All cut-offs for these criteria were progressively relaxed across iterations (see below). This  
354 approach allowed the identification of additional hits while iteratively strengthening the PSSM,  
355 reducing false positives. Each hit was extended by ±20 flanking residues for subsequent  
356 homology searches, and redundant sequences were removed. Each hit was then paired with  
357 the bait sequence (in this study, the human actin sequence) and saved as a separate FASTA  
358 file, formatted for direct compatibility with ColabFold.

359 For each hit, multiple sequence alignments (MSAs) were generated using **jackhmmer**<sup>44</sup> with  
360 the UniRef90 database. The following jackhmmer parameters were applied: number of  
361 iterations: 5, e-value: 1e-5, no f1 or f2 filter (Original AF2 code: number of iterations: 1, e-  
362 value: 1e-5, f1: 0.0005. f2: 0.00005). The modified jackhmmer parameters improved the  
363 number of sequences retrieved, likely enhancing detection of more distant homologs.  
364 Additionally, parallelization was implemented to process multiple hits simultaneously,

365 significantly speeding up the alignment step. The sto-file for the bait sequence was constructed  
366 in the same manner. Output alignments were reformatted to A3M format using the **HH-suite's**  
367 **reformat.pl**<sup>94</sup> script to ensure compatibility with downstream structure prediction tools.  
368 Alignments were sorted and combined to meet AlphaFold2 Multimer input criteria.

369 **2. ColabFold looped**

370 The **ColabFold\_looped.ipynb** notebook, originally developed by the Steinegger lab<sup>95</sup>, was  
371 modified to enable batch processing and the integration of custom MSAs, making it more  
372 suitable for the SLiMFold workflow. These modifications were designed to streamline the  
373 process and enhance flexibility when handling multiple input sequences. In the modified  
374 version, the notebook was adapted to loop through all FASTA-files in a specified folder, such  
375 as one located in Google Drive. This automation allowed for seamless processing of multiple  
376 sequences without the need for manual input, significantly improving the workflow's efficiency.  
377 Additionally, the modified notebook incorporated the ability to retrieve precomputed A3M files  
378 from another designated folder. These alignments, created during the Prerun.ipynb step, were  
379 matched to their corresponding FASTA-files based on their names. This ensured accurate  
380 integration of the custom MSAs into the ColabFold predictions. To manage outputs effectively,  
381 the notebook allowed users to specify a folder for storing results. This organizational setup  
382 made it easier to handle and analyze the results of large-scale computations.

383 Compared to the original ColabFold batch notebook, these modifications introduced enhanced  
384 flexibility by supporting custom MSAs and allowing adjustments to the number of seeds used  
385 in the AlphaFold2 predictions.

386 **3. Postanalysis**

387 The post-analysis step was performed using the **Postanalysis.ipynb** script, which  
388 systematically processed and analyzed the outputs from the SLiMFold pipeline. This step  
389 integrated sequence and structural data to evaluate the conformational and functional  
390 relevance of candidate F-actin-binding SLiMs. The pLDDT, pTM, and ipTM scores were  
391 extracted to assess prediction confidence and interaction reliability of each predicted structure.  
392 Structures with ipTM scores below 0.6 were excluded from further analysis, ensuring a focus  
393 on high-confidence predictions. Each remaining structure was aligned to a reference PDB file  
394 (in this study, the ITPKA-actin complex) to evaluate conformational similarity.

395

396 The **root-mean-square deviation (RMSD)** between the alpha carbon (C $\alpha$ ) atoms of the  
397 predicted structure and the reference structure at the motif positions (P1 to P9) was calculated  
398 to quantify structural similarity. RMSD was computed as:

399

$$\text{RMSD} = \frac{1}{N} \sum_{i=1}^N (x_i - x_{ref})^2$$

400 where  $N$  is the number of aligned residues,  $x_i$  represents the atomic coordinates of a residue  
401 in the predicted structure, and  $x_{ref}$  represents the corresponding coordinates in the reference  
402 structure.

403

404 Angular analysis was performed using vector-based calculations, where the spatial  
405 coordinates of the alpha carbon (Ca) atoms of key residues in the SLiM (P1 to P9) were used  
406 to define vectors representing the orientation of the motif. Two angles, **phi** ( $\varphi$ , azimuthal angle  
407 in the x-y plane) and **theta** ( $\theta$ , polar angle relative to the z-axis), were calculated to quantify  
408 the motif's orientation relative to the reference vector:

409

$$\varphi = \arctan\left(\frac{y}{x}\right) \quad \theta = \arccos\left(\frac{z}{|\nu|}\right)$$

410 where  $x$  and  $y$  are the coordinates of the vector projection in the x-y plane and where  $z$  is the  
411 z-coordinate of the vector and  $|\nu|$  is the magnitude of the vector. Helix polarity was also  
412 calculated to capture the directionality of the predicted motif's structural alignment. The **delta**  
413 **phi** ( $\Delta_\varphi$ ) and **delta theta** ( $\Delta_\theta$ ) values, representing the differences between the angles of the  
414 predicted and reference structures, were calculated for each candidate SLiM. These metrics,  
415 along with RMSD and polarity, provided a comprehensive structural profile for clustering.

416

417 Clustering was performed using the HDBSCAN<sup>45</sup> algorithm, leveraging RMSD,  $\Delta_\varphi$ ,  $\Delta_\theta$ , and  
418 polarity as input features. The clustering parameters, including minimum cluster size and  
419 minimum samples, were optimized using the following metrics:

- 420
- **Silhouette Score:** Evaluates cluster separation and cohesion.
  - **Davies-Bouldin Index:** Measures intra-cluster similarity relative to inter-cluster  
422 separation.
  - **Calinski-Harabasz Index:** Assesses the ratio of between-cluster dispersion to within-  
424 cluster dispersion.

425 Optimal clustering parameters were selected based on these indices, ensuring robust and  
426 meaningful grouping of structurally similar SLiMs. For further analysis, all structures belonging  
427 to a single cluster were exported as a PyMOL session file (.pml), enabling manual inspection  
428 and visualization. For each cluster, the corresponding sequences were compiled into a FASTA  
429 file. These sequences were used to generate sequence logos<sup>96</sup>, highlighting conserved

430 residues and identifying potential functional motifs. Additionally, each sequence was mapped  
431 to its corresponding gene using the NCBI database. This mapping facilitated gene ontology  
432 (GO) enrichment analysis, allowing functional insights into the biological roles of the identified  
433 SLiMs.

434

#### 435 **Cloning strategies**

436 All constructs were generated via PCR-based cloning using high-fidelity polymerases (Q5 or  
437 Phusion; M0491S or M0530S, New England Biolabs Inc., Massachusetts, USA) following the  
438 manufacturer's instructions. For inserting longer DNA fragments such as full-length protein  
439 sequences, we employed T4 SLIC<sup>97</sup> (Sequence and Ligation Independent Cloning) (T4 DNA  
440 Polymerase; M0203S, New England Biolabs Inc., Massachusetts, USA), which relies on ~30  
441 nucleotide overlaps between vector and insert for seamless assembly. Short peptides or  
442 specific mutations were introduced using a "QuickChange-like" site-directed mutagenesis  
443 protocol, wherein primer pairs incorporated short (8–12 nt) overlaps at their 5' ends; the PCR  
444 products were subsequently treated with DpnI (R0176S; New England Biolabs Inc.,  
445 Massachusetts, USA) to remove the template and then transformed into *E. coli* XL1-Blue  
446 (200249, Agilent Technologies, Inc., California, USA). Alternatively, the PCR products were  
447 processed using the KLD (Kinase–Ligase–DpnI) enzyme mix (M0554S, New England Biolabs  
448 Inc., Massachusetts, USA) to remove the template and ligate the new amplicon. For bacterial  
449 expression, PCR products were cloned into pSF421-based expression vectors (e.g.,  
450 pSF421\_10xHis\_GFP\_TEV), while for eukaryotic expression in mammalian cells (e.g.,  
451 H1299), target genes were inserted into an mEGFP-N1 backbone. All final plasmids were  
452 verified by Sanger sequencing (Microsynth Seqlab GmbH, Göttingen, Germany). Verified  
453 constructs were subsequently transformed into *E. coli* Rosetta™ (DE3) (Novagen, Merck  
454 KGaA, Darmstadt, Germany) for bacterial protein expression or transfected into mammalian  
455 cells. Complete plasmid lists, vector maps, sequencing results, and primer sequences are  
456 provided in Supplementary Tables 2 and 3 and Source Data.

457

#### 458 **Purification of Actin**

459 Actin was prepared from Gallus gallus (chicken) skeletal muscle as described in reference<sup>98</sup>.  
460 The final purification step was performed using a HiLoad 16/600 Superdex 200 column  
461 equilibrated with G-actin buffer (5 mM Tris-HCl, pH 7.5, 0.2 mM CaCl<sub>2</sub>, 0.5 mM DTT and  
462 0.2 mM ATP).

463

464 **Expression and Purification of ITPKA and GFP-Peptides**

465 All constructs were expressed in *E. coli* Rosetta™ (DE3) competent cells (Novagen, Merck  
466 KGaA, Darmstadt, Germany). Cells were grown in Terrific Broth (TB) medium at 37°C to an  
467 optical density ( $OD_{600}$ ) between 0.6 and 1.0. Protein expression was induced with 0.2 mM  
468 isopropyl β-D-1-thiogalactopyranoside (IPTG) at 18°C for 16 hours for ITPKA and with 0.2 mM  
469 isopropyl β-D-1-thiogalactopyranoside (IPTG) at 37°C for 4 hours for the GFP-Peptides. After  
470 induction, cells were harvested by centrifugation at 3,000 × g for 20 minutes at 4°C. The cell  
471 pellets were resuspended in cold phosphate-buffered saline (PBS) buffer, centrifuged at 2,000  
472 × g for 30 minutes at 4°C, flash-frozen in liquid nitrogen, and stored at -80°C.

473 For protein purification, the cell pellets were resuspended in ice-cold Buffer A (50 mM Tris-  
474 HCl, pH 7.4, 400 mM NaCl, 3 mM MgCl<sub>2</sub> 1 mM β-mercaptoethanol for ITPKA and 50 mM Tris-  
475 HCl, pH 7.4, 300 mM NaCl, 1 mM β-mercaptoethanol for GFP-Peptides) and homogenized  
476 using an IKA® ULTRA-TURRAX® disperser (IKA-Werke GmbH & Co. KG, Staufen, Germany).  
477 DNase I was added, and the cells were lysed with a Constant Cell Disruption System (Constant  
478 Systems Limited, Daventry, UK) at 1.8 kbar. Following lysis, phenylmethylsulfonyl fluoride  
479 (PMSF) was added to a final concentration of 1 mM and imidazole to a final concentration of  
480 25 mM. Cell debris was removed by centrifugation at 43,000 × g for 30 minutes at 4°C, and  
481 the supernatant was incubated with Ni-NTA agarose resin (SERVA Electrophoresis GmbH,  
482 Heidelberg, Germany) for 30 minutes at 4°C. The bound proteins were eluted using a gradient  
483 of Buffer B (Buffer A with 500 mM imidazole). Fractions were analyzed by SDS-PAGE, and  
484 those with >90% purity were pooled and then dialyzed overnight at 4°C in Buffer A.

485 For the ITPKA protein, an additional cleavage step was performed to remove His tag. The  
486 pooled protein fractions were dialyzed overnight at 4°C in the presence of TEV protease, at a  
487 ratio of 1 mg TEV protease per 40 mg protein substrate, in Buffer A. Following dialysis, the  
488 cleaved protein was separated from the tags and TEV protease by reverse immobilized metal  
489 affinity chromatography (IMAC) using a Ni<sup>2+</sup>-NTA column (Bio-Rad Laboratories, California,  
490 USA) on an NGC™ Liquid Chromatography System (Bio-Rad Laboratories, California, USA).

491 Subsequently, the pooled reversed IMAC fractions (for ITPKA) or the dialyzed proteins (for  
492 GFP Peptides) were concentrated to 0.5–2 mL using Amicon® Ultra Centrifugal Filters (Merck-  
493 Millipore, Massachusetts, USA) and further purified by size-exclusion chromatography using a  
494 HiLoad Superdex 16/600 200pg Gel Filtration Column (Cytiva, Massachusetts, USA) on an  
495 NGC™ Liquid Chromatography System (Bio-Rad Laboratories, California, USA), equilibrated  
496 with Buffer D (50 mM Tris-HCl, pH 7.4, 150 mM NaCl, 3 mM MgCl<sub>2</sub> 1 mM β-mercaptoethanol  
497 for ITPKA and 50 mM Tris-HCl, pH 7.4, 150 mM NaCl, 1 mM β-mercaptoethanol for GFP-  
498 Peptides) . The peak fractions were concentrated, aliquoted, then flash-frozen in liquid  
499 nitrogen, and stored at -80°C.

500

501 **Cryo-EM data acquisition and processing**

502 We initiated all sample preparations using frozen aliquots of G-actin. To convert G-actin into  
503 F-actin, we first thawed the samples and performed centrifugation at 100,000 x g for 30 minutes  
504 to eliminate potential aggregates. The polymerization process involved adding F buffer to  
505 achieve a final concentration of 20 mM Tris-HCl pH 7.5, 100 mM KCl, 2 mM MgCl<sub>2</sub>, 0.5 mM  
506 ATP, 1 mM EGTA, and 1 mM DTT, followed by incubation for one hour at room temperature.  
507 Subsequently, we collected the filaments by centrifuging at 100,000 x g for one hour at 4°C  
508 and resuspended them in F buffer supplemented with Phalloidin at twice the molar  
509 concentration of F-actin.

510 For cryo-EM grid preparation, we used Quantifoil 200-mesh 2.0/1.0 holey carbon grids.  
511 Specifically, for Phalloidin-stabilized F-actin, we applied 3.5 µl of 1 µM solution onto glow-  
512 discharged grids. For the Phalloidin-stabilized F-actin-ITPKA complex, we initially applied 2 µl  
513 of 1 µM Phalloidin-stabilized F-actin to the grids. Subsequently, we added 2 µl of 10 µM ITPKA  
514 and mixed it directly on the grids immediately before plunge-freezing in a liquid ethane/propane  
515 mixture using a Vitrobot Mark IV (FEI). Datasets were collected on an FEI Titan Krios (300 KV;  
516 Gatan K3 camera; pixel size: 0.826 Å; dose per frame: 1.4; defocus range: 0.8 to 3.0 µm).

517 Single-particle helical reconstruction was performed using Relion 4<sup>99</sup>. Movies were firstly  
518 motion-corrected using MotionCor2<sup>100</sup>, and then the contrast transfer function (CTF) estimation  
519 was done using CTFFIND4<sup>101</sup>. Particle segments picking model was trained in cryolo 1.7<sup>102</sup>.  
520 The helical segments were extracted into 360 × 360 boxes and the junk segments were  
521 excluded after 2D classification. The initial helical parameters of a helical rise of 27.3 Å and a  
522 helical twist of -166.5° were applied for 3D classification and autorefinement in Relion 4.0.  
523 Overall, gold-standard resolution (Fourier shell correlation = 0.143) was calculated in Relion  
524 4.0. The statistics for data collection and processing are listed in Supplementary Table 4.

525

526 **Model building and refinement**

527 Previously published models of phalloidin bound F-actin (PDB: 6T20<sup>103</sup>, 7BTI<sup>40</sup>), and the  
528 AlphaFold2 structure of ITPKA were used as initial models. Models were initially built in  
529 ChimeraX 1.7<sup>104</sup>, and further refined against the cryo-EM maps using ISOLDE<sup>105</sup>, and real  
530 space refinement in Phenix<sup>106</sup>. The detailed model information and validation statistics for final  
531 models are described in Supplementary Table 4.

532

533 **Cell culture**

534 NCI-H1299 (H1299) cells were kindly provided by Cagatay Günes (Hamburg, Germany). For  
535 detailed cellular characteristics, refer to the American Type Culture Collection (ATCC,  
536 Rockville, USA). The cells were cultured in Dulbecco's Modified Eagle's Medium (DMEM)  
537 supplemented with 10% (v/v) fetal calf serum (FCS), 4 mM L-glutamine, 100 µg/ml  
538 streptomycin, and 100 U/ml penicillin. The culturing conditions were rigorously maintained to  
539 ensure optimal growth and viability. Additionally, the cells were tested regularly for  
540 mycoplasma contamination to ensure experiments were conducted with mycoplasma-free  
541 cells.

542 Primary human monocytes were isolated from buffy coats (kindly provided by Frank Bentzien,  
543 Transfusion Medicine, UKE, Hamburg, Germany). 20 ml blood was coated on 15 ml  
544 Lymphocyte Separation Medium 1077 (PromoCell, Heidelberg, Germany) and centrifuged for  
545 30 min at 4°C and 460×g. Buffy coats were transferred to a new 50 ml Falcon tube and filled  
546 up to 50 ml with cold RPMI (Gibco, Paisley, UK). Leukocyte fractions were washed twice in  
547 RPMI and centrifuged for 10 min, as described above. Enriched leukocytes were resuspended  
548 in 400 µl monocyte buffer (5 mM EDTA and 0.5% human serum albumin in Dulbecco's PBS  
549 [DPBS], pH 7.4), mixed with 100 µl of magnetic beads suspension coupled to anti-CD14  
550 antibodies (Miltenyi Biotec, Bergisch Gladbach, Germany) and incubated for 15 min on ice.  
551 The mixture was subsequently loaded onto Separation columns LS (Miltenyi Biotec, Bergisch  
552 Gladbach, Germany) that were previously placed in a magnetic holder and equilibrated with  
553 500 µl cold monocyte buffer. Trapped CD14+ monocytes were washed on column with 500 µl  
554 monocyte buffer and then eluted with 1ml monocyte buffer into 15 ml cold RPMI after removal  
555 from the magnets. After centrifugation for 10 min at 4°C and 460×g, the supernatant was  
556 removed and cells were resuspended in 40 ml RPMI and seeded on a 6-well plate (Sarstedt,  
557 Nuembrech, Germany) at a density of 2\*10<sup>6</sup> cells per well. After adhesion of monocytes for  
558 1h, RPMI medium was replaced by 2 ml monocyte culture medium (RPMI substituted with 20%  
559 human serum and 1% penicillin/streptomycin (Sigma-Aldrich, Missouri, USA). Monocytes were  
560 cultivated in an incubator at 37°C, 5% CO<sub>2</sub>, and 90% humidity. Isolated monocytes were  
561 differentiated for at least 6 days.

562

563 **Transfection of Cells**

564 For H1299 cells, a total of 2.5 × 10<sup>4</sup> cells were seeded into 8 well chamber slides (Ibidi,  
565 Gräfelfing, Germany). After 16 h, the cells were transfected with 0.5 µg with any mEGFP-N1-  
566 Peptide or mEGFP-N1-FL-Proteins using the K2® Transfection Reagent (T060-0.75, Biontex  
567 Laboratories GmbH, München, Germany) according to the manufacturer's instructions. After

568 24 h, the cells were fixed with 4% paraformaldehyde/4% sucrose, stained with rhodamine-  
569 conjugated phalloidin (ab235138, Abcam Limited., Cambridge, UK), and analyzed by  
570 fluorescence microscopy using the Olympus IXplore Live microscope imaging system and the  
571 FV3000 confocal laser scanning microscope (Olympus Corporation, Tokyo, Japan).

572 Macrophages were detached by incubation of Accutase (Invitrogen, Massachusetts, USA) for  
573 at least 30 min in culturing conditions. Cells were collected with monocyte culture medium,  
574 washed in PBS pH 7.3 and resuspended in R-Buffer (at a concentration of 106 cells per 100  
575 µl buffer, 10 µg DNA), provided by the Neon Transfection System (Invitrogen, Massachusetts,  
576 USA). Macrophages were transiently transfected with plasmid DNA with the following settings:  
577 voltage 1,000 V; width 40 ms, and 2 pulses. Transfected cells were resuspended in RPMI and  
578 seeded on 12-mm glass coverslips (105 cells per coverslip). The cells were left to adhere for  
579 1 h at culturing conditions. Thereafter, 1 ml of monocyte culture medium was added, and cells  
580 were incubated overnight.

581

## 582 **Immunofluorescence and microscopy**

583 Cells were fixed for 10 min in 3.7% formaldehyde in PBS, and permeabilized for 10 min in PBS  
584 containing 0.5% TritonX-100. Thereafter cells were incubated for 60 min in blocking solution  
585 (2% BSA in PBS) with 1:400 phalloidin-568. Cells were washed three times in PBS and  
586 mounted on glass slides with FluoromountG (Invitrogen Massachusetts, USA) containing DAPI  
587 (Sigma-Aldrich, Missouri, USA). Images of fixed samples were acquired with a confocal laser-  
588 scanning microscope Olympus FV3000 equipped with an 60x UPlanApo HR Oil objective and  
589 Olympus FV-3000 software.

590

## 591 **Poji Macro Analysis**

592 Semi-automated Poji analysis was performed as previously described in reference<sup>107</sup>. Profile  
593 analysis was performed on ROI of transfected cells with podosomes defined by phalloidin-568  
594 staining with a circle size of single isolated podosomes of 25 pixels. For more detailed  
595 information, see <https://github.com/roherzog/Poji>.

596

## 597 **Cosedimentation assay and $K_D$ Determination**

598 The dissociation constant ( $K_D$ ) and binding strength of the interaction between the actin-  
599 binding protein (ABP) and filamentous actin (F-actin) were determined using an F-actin  
600 cosedimentation assay.

601 For this, preparations were made using frozen aliquots of G-actin. To convert G-actin into F-  
602 actin, the samples were thawed and centrifuged at 100,000 × g for 30 minutes to eliminate  
603 potential aggregates. The polymerization process involved adding F-buffer to achieve a final  
604 concentration of 20 mM Tris (pH 7.5), 100 mM KCl, 2 mM MgCl<sub>2</sub>, 0.5 mM ATP, 1 mM EGTA,  
605 and 1 mM DTT. The samples were then incubated for one hour at room temperature. The  
606 resulting F-actin was mixed with an equivalent amount of ABP and incubated for one hour at  
607 room temperature before cosedimentation at 100,000 × g for 30 minutes. Pellet and  
608 supernatant fractions were resuspended in sample buffer, heated at 95 °C for 15 min, and  
609 analyzed by SDS-PAGE and Western blot or Coomassie staining as detailed below.

610 For ABPs exhibiting relatively **low affinity** ( $K_D > [ABP]$ ), such that free actin remains largely  
611 undepleted), we measured only the pellet fraction by Western blot and plotted densitometry  
612 (D) as a function of the total actin concentration  $[Actin]_{total}$ . These data were fit in GraphPad  
613 Prism using the “One site – Specific binding” hyperbolic model:

$$614 \quad D = \frac{B_{max} \times [Actin]_{total}}{K_D + ([Actin]_{total})}$$

615 Here,  $B_{max}$  corresponds to the maximal densitometry signal at saturation.

616 For **higher-affinity** ABPs ( $K_D < [ABP]$ ), the free actin can be substantially depleted, so a  
617 simple hyperbolic fit may be inaccurate. In these cases, we quantified both pellet and  
618 supernatant fractions by SDS-PAGE to determine the fraction of total ABP bound, Y. We then  
619 fit Y against  $[Actin]_{total}$  using the „Quadratic” (or “Tight Binding”) model<sup>108</sup>:

$$620 \quad Y = \frac{[ABP] [Actin]}{[ABP]_{total}}$$

$$621 \quad Y = \frac{[Actin]_{total} + [ABP] + K_D - \sqrt{([Actin]_{total} + [ABP] + K_D)^2 - 4 \cdot [ABP] \cdot [Actin]_{total}}}{2 \cdot [ABP]}$$

622 All experiments were performed in triplicate to ensure reproducibility. Varying concentrations  
623 of actin (0–120 μM) were incubated with a fixed concentration of ABP (4 μM). In each replicate,  
624 a negative control (0 μM actin) verified background signal. For low-affinity peptides, blot  
625 exposures were selected to remain in the linear range of detection, and densitometry signals  
626 (D) were directly used in the hyperbolic fit. For high-affinity assays, we confirmed mass balance  
627 by checking that pellet + supernatant matched the total ABP added. Nonlinear regression in  
628 GraphPad Prism was used to extract  $K_D$  and  $B_{max}$ .

629 For the binding strength determination of USP54 and SHROOM3 mutants (M1, M2, M3, and  
630 M4), the proteins were employed at a final concentration of 4 μM with F-actin at 12 μM.  
631 Densitometric analysis was performed on the Western blot results, quantifying the signal

632 intensity of the bound ABP in the pellet fraction to assess differences in binding strength among  
633 the mutants. The densitometry values were corrected by subtraction of the negative control  
634 (SFM with 0 µM Actin).

635

### 636 **SDS-PAGE and Western Blotting**

637 Equal volumes of samples were loaded onto 12% polyacrylamide gels for SDS-PAGE.  
638 Electrophoresis was performed at 120 V until the dye front reached the bottom of the gel. SDS-  
639 PAGE was transferred onto nitrocellulose membranes using a wet transfer system at 60 V for  
640 90 minutes in 1x blot buffer. Membranes were blocked with 5% (w/v) non-fat dry milk or 5%  
641 BSA in Tris-buffered saline with Tween 20 (TBST) for 1 hour at room temperature to block  
642 nonspecific binding sites. The membranes were incubated overnight at 4°C with the primary  
643 antibody specific to GFP (mouse anti-GFP, 1:1,500, Article No. 11814460001, Roche Applied  
644 Science, Penzberg, Germany) or actin (rabbit anti-actin, 1:10,000, Article No. A2066, Sigma  
645 Aldrich, St. Louis, MO, USA) diluted in blocking buffer. After three washes with TBST, the  
646 membranes were incubated for 1 hour at room temperature with the appropriate HRP-  
647 conjugated secondary antibody. Goat anti-mouse secondary antibody was used for GFP  
648 detection (1:10,000 dilution in TBST), while goat anti-rabbit secondary antibody was used for  
649 actin detection (1:10,000). Protein bands were detected using a chemiluminescence reagent  
650 (Cytiva Amersham™ ECL™ Prime Western Blot Detection Reagent) and imaged using the  
651 INTAS ECL CHEMOCAM (INTAS Science Imaging Instruments GmbH, Göttingen, Germany).  
652 Band intensities were analyzed using ImageJ<sup>109</sup>.

653

### 654 **Position specific frequency matrix (PSFM)**

655 We developed a pipeline for generating position-specific frequency matrices (PSFMs) that  
656 quantify amino acid conservation at each position across a set of sequences, focusing  
657 specifically on peptides with high affinity or strong colocalization. Multiple sequence alignments  
658 (MSAs) derived from SLiMFold's jackhmmer output were manually curated to remove  
659 alignments with names indicating different proteins, ensuring retention of only true homologs.  
660 These curated MSAs served as input for generating individual frequency tables for each  
661 peptide, which were then averaged to account for variations in the number of homologous  
662 sequences. A 23×N matrix (where N is the sequence length) was generated, with each element  
663 representing the proportion of a specific amino acid at a given position. To reduce skewness  
664 in the data and emphasize subtle conservation trends, a square root transformation was  
665 applied to the matrix. Heatmaps of the PSFMs were visualized using matplotlib, with conserved

666 positions annotated and residue indices labeled for interpretation. Detailed code is provided in  
667 the reference<sup>110</sup>.

668

## 669 **Phylogenetic and Motif Analysis**

670 To investigate the evolutionary history of F-actin binding motif-containing proteins and their  
671 isoforms, we conducted a comprehensive phylogenetic analysis. Orthologous sequences were  
672 retrieved from OrthoDB<sup>111</sup> and aligned using DECIPHER<sup>112</sup> (100 iterations, 200 refinements).  
673 Maximum likelihood phylogenetic trees were constructed with IQ-TREE 2<sup>113</sup> (WAG+G model,  
674 1000 ultrafast bootstraps). Isoform sequences were identified and filtered based on header  
675 annotations, and their phylogenetic clustering was visualized. Taxonomic information was  
676 incorporated to determine the MRCA of isoform clusters. F-actin binding motifs were extracted  
677 using regular expressions and filtered based on predicted disorder (IUPRED<sup>43</sup>), anchor regions  
678 (ANCHOR<sup>42</sup>), and random coil propensity (PSIPRED<sup>41</sup>). Position-Specific Scoring Matrices  
679 (PSSMs) were generated and iteratively used to refine motif identification. The MRCA of motif-  
680 containing sequences was determined using isoform-specific trees. Motif distribution was  
681 validated by mapping motifs to a taxon-based tree. Motif development across isoforms and  
682 taxonomic classes was analyzed using frequency matrices. Sequence logos<sup>96</sup> were generated  
683 from PSSMs. For nucleotide-level analyses, corresponding DNA sequences were retrieved  
684 from NCBI, filtered for ambiguous bases and stop codons, and codon-aligned using PRANK<sup>114</sup>.  
685 Phylogenetic trees were inferred with IQ-TREE 2<sup>113</sup> (GTR+G model), and dN/dS analysis was  
686 performed using HyPhy<sup>115</sup>. Detailed code and parameter settings are provided in the Source  
687 Data.

688

## 689 **GO Enrichment analysis**

690 To elucidate the biological functions and cellular components associated with Short Linear F-  
691 actin Binding Motif (SFM)-containing proteins, we performed Gene Ontology (GO) enrichment  
692 analysis using ShinyGO<sup>116</sup>. The analysis aimed to identify overrepresented GO terms within  
693 three primary categories: Biological Process (BP), Cellular Component (CC), and Molecular  
694 Function (MF). We compiled a comprehensive list of SFM-containing proteins identified in this  
695 study as the query set. Utilizing ShinyGO with its standard parameters, we input the query set  
696 to perform the enrichment analysis. The analysis employed the default settings for multiple  
697 testing correction, including the False Discovery Rate (FDR), ensuring that only GO terms with  
698 an adjusted p-value below 0.05 were considered significantly enriched.

699

700 **AlphaMissense**

701 For each of the 12 proteins examined in this study, the AlphaMissense pathogenicity score<sup>47</sup>  
702 was retrieved using the canonical UniProt ID. The relevant amino acid positions were then  
703 manually aligned based on the SFM motif coordinates. Residues flanking the motif (positions  
704 –30 to –20 and +30 to +40) served as control values for comparative analysis. After extracting  
705 the AlphaMissense scores for all 12 proteins, the mean score at each aligned position was  
706 calculated and the standard error of the mean (SEM) determined. Statistical evaluation of  
707 differences between motif residues and the flanking control positions was performed via one-  
708 way ANOVA with multiple comparisons.

709

710 **Data availability**

711 Coordinates and cryo-EM maps for the F-actin structure have been deposited in the Electron  
712 Microscopy Data Bank (EMDB) under accession code EMD-18866, with corresponding Protein  
713 Data Bank (PDB) entry 8R3H. The F-actin–ITPKA complex has been deposited in the EMDB  
714 under accession code EMD-18868 and in the PDB under accession code 8R3J. Additionally,  
715 PDB entries 6T20, 7BTI, and 7AD9 were used for structural comparisons. The SLiMFold  
716 pipeline code is available at <https://github.com/thp42/SLiMFold>, and the PSFM code is  
717 provided at <https://github.com/thp42/PSFM>. Source data underlying this study are provided  
718 with the paper.

719

720 **Acknowledgements**

721 We thank Christine Blechner and Andrea Mordhorst for excellent technical assistance. We also  
722 acknowledge Christian Dahlstroem (AG Windhorst, Universitätsklinikum Hamburg-Eppendorf)  
723 Nicholas Kley and Joel Fauser (AG Itzen, Universitätsklinikum Hamburg-Eppendorf) for  
724 continuous support. We are grateful to Frank Bentzien (Transfusion Medicine,  
725 Universitätsklinikum Hamburg-Eppendorf) for providing buffy coats, and to Robert Herzog and  
726 Pasquale Cervero for help in validating podosome detection. We thank Malik Alawi, Philipp  
727 Dirksen and Susanne Dobler for critical evaluation of our phylogenetic analysis. We further  
728 appreciate the support of the UKE Microscopy Imaging Facility (UMIF, DFG code RI\_00489  
729 and INST 152/933-1) for advanced microscopy access and image analysis, as well as Martin  
730 Aepfelbacher and Aymelt Itzen for continuous support. This project was funded by Erich und  
731 Gertrud Roggenbuck-Stiftung (to S.W. and T.P.). It is part of the doctoral thesis of K.S. and  
732 was additionally supported by the Deutsche Forschungsgemeinschaft (RTG2771/P4, to S.L.).

733

734

735 **References**

- 736 1. Pollard, T. D. & Borisy, G. G. Cellular Motility Driven by Assembly and Disassembly of  
737 Actin Filaments. *Cell* **112**, 453–465 (2003).
- 738 2. Heasman, S. J. & Ridley, A. J. Mammalian Rho GTPases: new insights into their  
739 functions from in vivo studies. *Nat Rev Mol Cell Biol* **9**, 690–701 (2008).
- 740 3. Hall, A. Rho GTPases and the Actin Cytoskeleton. *Science* **279**, 509–514 (1998).
- 741 4. Fox, J. W. *et al.* Mutations in filamin 1 Prevent Migration of Cerebral Cortical Neurons in  
742 Human Periventricular Heterotopia. *Neuron* **21**, 1315–1325 (1998).
- 743 5. Motley, W. W., Züchner, S. & Scherer, S. S. Isoform-specific loss of dystonin causes  
744 hereditary motor and sensory neuropathy. *Neurol Genet* **6**, e496 (2020).
- 745 6. Standing, A. S. I. *et al.* Autoinflammatory periodic fever, immunodeficiency, and  
746 thrombocytopenia (PFIT) caused by mutation in actin-regulatory gene *WDR1*. *Journal of  
747 Experimental Medicine* **214**, 59–71 (2017).
- 748 7. Kahr, W. H. A. *et al.* Loss of the Arp2/3 complex component ARPC1B causes platelet  
749 abnormalities and predisposes to inflammatory disease. *Nat Commun* **8**, 14816 (2017).
- 750 8. Haffner, M. C. *et al.* AIM1 is an actin-binding protein that suppresses cell migration and  
751 micrometastatic dissemination. *Nat Commun* **8**, 142 (2017).
- 752 9. Dominguez, R. Actin-binding proteins – a unifying hypothesis. *Trends in Biochemical  
753 Sciences* **29**, 572–578 (2004).
- 754 10. Köster, J.-D. *et al.* Inositol-1,4,5-trisphosphate-3-kinase-A controls morphology of  
755 hippocampal dendritic spines. *Cellular Signalling* **28**, 83–90 (2016).
- 756 11. Shatskiy, D., Sivan, A., Wedlich-Söldner, R. & Belyy, A. Structure of the F-tractin–F-actin  
757 complex. *Journal of Cell Biology* **224**, e202409192 (2025).
- 758 12. Dunker, A. K. *et al.* Intrinsically disordered protein. *Journal of Molecular Graphics and  
759 Modelling* **19**, 26–59 (2001).
- 760 13. Wright, P. E. & Dyson, H. J. Intrinsically unstructured proteins: re-assessing the protein  
761 structure-function paradigm. *Journal of Molecular Biology* **293**, 321–331 (1999).

- 762 14. Uversky, V. N., Gillespie, J. R. & Fink, A. L. Why are ?natively unfolded? proteins  
763 unstructured under physiologic conditions? *Proteins* **41**, 415–427 (2000).
- 764 15. Tompa, P. Intrinsically unstructured proteins. *Trends in Biochemical Sciences* **27**, 527–  
765 533 (2002).
- 766 16. Dyson, H. J. & Wright, P. E. Intrinsically unstructured proteins and their functions. *Nat  
767 Rev Mol Cell Biol* **6**, 197–208 (2005).
- 768 17. Xie, H. *et al.* Functional Anthology of Intrinsic Disorder. 1. Biological Processes and  
769 Functions of Proteins with Long Disordered Regions. *J. Proteome Res.* **6**, 1882–1898  
770 (2007).
- 771 18. Galea, C. A., Wang, Y., Sivakolundu, S. G. & Kriwacki, R. W. Regulation of Cell Division  
772 by Intrinsically Unstructured Proteins: Intrinsic Flexibility, Modularity, and Signaling  
773 Conduits. *Biochemistry* **47**, 7598–7609 (2008).
- 774 19. Gsponer, J. & Madan Babu, M. The rules of disorder or why disorder rules. *Progress in  
775 Biophysics and Molecular Biology* **99**, 94–103 (2009).
- 776 20. Tompa, P. Unstructural biology coming of age. *Current Opinion in Structural Biology* **21**,  
777 419–425 (2011).
- 778 21. Babu, M. M., van der Lee, R., de Groot, N. S. & Gsponer, J. Intrinsically disordered  
779 proteins: regulation and disease. *Current Opinion in Structural Biology* **21**, 432–440  
780 (2011).
- 781 22. Dinkel, H. *et al.* The eukaryotic linear motif resource ELM: 10 years and counting. *Nucl.  
782 Acids Res.* **42**, D259–D266 (2014).
- 783 23. Davey, N. E. *et al.* Attributes of short linear motifs. *Mol. BioSyst.* **8**, 268–281 (2012).
- 784 24. Mohan, A. *et al.* Analysis of Molecular Recognition Features (MoRFs). *Journal of  
785 Molecular Biology* **362**, 1043–1059 (2006).
- 786 25. Mi, T. *et al.* Minimotif Miner 3.0: database expansion and significantly improved reduction  
787 of false-positive predictions from consensus sequences. *Nucleic Acids Research* **40**,  
788 D252–D260 (2012).

- 789 26. Chereau, D. *et al.* Actin-bound structures of Wiskott–Aldrich syndrome protein (WASP)-  
790 homology domain 2 and the implications for filament assembly. *Proc. Natl. Acad. Sci.  
791 U.S.A.* **102**, 16644–16649 (2005).
- 792 27. Marguet, F. *et al.* Association of fingerprint bodies with rods in a case with mutations in  
793 the LMOD3 gene. *Neuromuscular Disorders* **30**, 207–212 (2020).
- 794 28. Schatz, U. A. *et al.* Evidence of mild founder *LMOD3* mutations causing nemaline  
795 myopathy 10 in Germany and Austria. *Neurology* **91**, e1690–e1694 (2018).
- 796 29. Liverman, A. D. B. *et al.* Arp2/3-independent assembly of actin by *Vibrio* type III effector  
797 VopL. *Proc. Natl. Acad. Sci. U.S.A.* **104**, 17117–17122 (2007).
- 798 30. Tam, V. C. *et al.* Functional Analysis of VopF Activity Required for Colonization in *Vibrio*  
799 *cholerae*. *mBio* **1**, e00289-10 (2010).
- 800 31. Wood, H. & Artsob, H. Spotted Fever Group Rickettsiae: A Brief Review and a Canadian  
801 Perspective: Spotted Fever Group Rickettsiae. *Zoonoses and Public Health* **59**, 65–79  
802 (2012).
- 803 32. Reed, S. C. O., Lamason, R. L., Risca, V. I., Abernathy, E. & Welch, M. D. Rickettsia  
804 Actin-Based Motility Occurs in Distinct Phases Mediated by Different Actin Nucleators.  
805 *Current Biology* **24**, 98–103 (2014).
- 806 33. Windhorst, S. *et al.* Inositol-1,4,5-trisphosphate 3-kinase A regulates dendritic  
807 morphology and shapes synaptic Ca<sup>2+</sup> transients. *Cellular Signalling* **24**, 750–757  
808 (2012).
- 809 34. Windhorst, S. *et al.* Inositol 1,4,5-Trisphosphate 3-Kinase-A Is a New Cell Motility-  
810 promoting Protein That Increases the Metastatic Potential of Tumor Cells by Two  
811 Functional Activities. *Journal of Biological Chemistry* **285**, 5541–5554 (2010).
- 812 35. Paraschiakos, T., Flat, W., Chen, Y., Kirchmair, J. & Windhorst, S. Mechanism of BIP-4  
813 mediated inhibition of InsP3Kinase-A. *Bioscience Reports* **41**, BSR20211259 (2021).
- 814 36. Ashour, D. J. *et al.* The catalytic domain of inositol-1,4,5-trisphosphate 3-kinase-a  
815 contributes to ITPKA-induced modulation of F-actin: Effect of Full Length ITPKA on Actin  
816 Structure. *Cytoskeleton* **72**, 93–100 (2015).

- 817 37. Küster, L. *et al.* The actin bundling activity of ITPKA mainly accounts for its migration-  
818 promoting effect in lung cancer cells. *Bioscience Reports* **43**, BSR20222150 (2023).
- 819 38. Melak, M., Plessner, M. & Grosse, R. Actin visualization at a glance. *Journal of Cell*  
820 *Science* jcs.189068 (2017) doi:10.1242/jcs.189068.
- 821 39. Belyy, A., Merino, F., Sitsel, O. & Raunser, S. Structure of the Lifeact-F-actin complex.  
822 *PLoS Biol* **18**, e3000925 (2020).
- 823 40. Kumari, A., Kesarwani, S., Javoor, M. G., Vinothkumar, K. R. & Sirajuddin, M. Structural  
824 insights into actin filament recognition by commonly used cellular actin markers. *EMBO J*  
825 **39**, (2020).
- 826 41. Buchan, D. W. A. & Jones, D. T. The PSIPRED Protein Analysis Workbench: 20 years  
827 on. *Nucleic Acids Res* **47**, W402–W407 (2019).
- 828 42. Dosztányi, Z., Mészáros, B. & Simon, I. ANCHOR: web server for predicting protein  
829 binding regions in disordered proteins. *Bioinformatics* **25**, 2745–2746 (2009).
- 830 43. Dosztányi, Z. Prediction of protein disorder based on IUPred. *Protein Sci* **27**, 331–340  
831 (2018).
- 832 44. Finn, R. D. *et al.* HMMER web server: 2015 update. *Nucleic Acids Res* **43**, W30-38  
833 (2015).
- 834 45. McInnes, L., Healy, J. & Astels, S. hdbSCAN: Hierarchical density based clustering. *JOSS*  
835 **2**, 205 (2017).
- 836 46. Linder, S., Cervero, P., Eddy, R. & Condeelis, J. Mechanisms and roles of podosomes  
837 and invadopodia. *Nat Rev Mol Cell Biol* (2022) doi:10.1038/s41580-022-00530-6.
- 838 47. Cheng, J. *et al.* Accurate proteome-wide missense variant effect prediction with  
839 AlphaMissense. *Science* **381**, eadg7492 (2023).
- 840 48. Arai, A., Spencer, J. A. & Olson, E. N. STARS, a Striated Muscle Activator of Rho  
841 Signaling and Serum Response Factor-dependent Transcription. *Journal of Biological*  
842 *Chemistry* **277**, 24453–24459 (2002).

- 843 49. Banerjee, J., Fischer, C. C. & Wedegaertner, P. B. The Amino Acid Motif L/I<sub>xx</sub>FE  
844 Defines a Novel Actin-Binding Sequence in PDZ-RhoGEF. *Biochemistry* **48**, 8032–8043  
845 (2009).
- 846 50. Zhan, Q. Q., Wong, S. S. & Wang, C. L. A calmodulin-binding peptide of caldesmon.  
847 *Journal of Biological Chemistry* **266**, 21810–21814 (1991).
- 848 51. D'Atri, F. & Citi, S. Cingulin interacts with F-actin in vitro. *FEBS Letters* **507**, 21–24  
849 (2001).
- 850 52. Scherer, A. N., Anand, N. S. & Koleske, A. J. Cortactin stabilization of actin requires  
851 actin-binding repeats and linker, is disrupted by specific substitutions, and is independent  
852 of nucleotide state. *Journal of Biological Chemistry* **293**, 13022–13032 (2018).
- 853 53. Marat, A. L., Ioannou, M. S. & McPherson, P. S. Connecdenn 3/DENND1C binds actin  
854 linking Rab35 activation to the actin cytoskeleton. *MBoC* **23**, 163–175 (2012).
- 855 54. Wang, X. *et al.* DIXDC1 isoform, I-DIXDC1, is a novel filamentous actin-binding protein.  
856 *Biochemical and Biophysical Research Communications* **347**, 22–30 (2006).
- 857 55. Hao, J.-J., Zhu, J., Zhou, K., Smith, N. & Zhan, X. The Coiled-coil Domain Is Required for  
858 HS1 to Bind to F-actin and Activate Arp2/3 Complex. *Journal of Biological Chemistry*  
859 **280**, 37988–37994 (2005).
- 860 56. Johnson, H. W. & Schell, M. J. Neuronal IP<sub>3</sub> 3-Kinase is an F-actin–bundling Protein:  
861 Role in Dendritic Targeting and Regulation of Spine Morphology. *MBoC* **20**, 5166–5180  
862 (2009).
- 863 57. Brehm, M. A., Schreiber, I., Bertsch, U., Wegner, A. & Mayr, G. W. Identification of the  
864 actin-binding domain of Ins(1,4,5) P 3 3-kinase isoform B (IP3K-B). *Biochemical Journal*  
865 **382**, 353–362 (2004).
- 866 58. Maul, R. S. *et al.* EPLIN regulates actin dynamics by cross-linking and stabilizing  
867 filaments. *The Journal of Cell Biology* **160**, 399–407 (2003).
- 868 59. Fauchereau, F. The RhoGAP activity of OPHN1, a new F-actin-binding protein, is  
869 negatively controlled by its amino-terminal domain. *Molecular and Cellular Neuroscience*  
870 **23**, 574–586 (2003).

- 871 60. Kelber, J. A. & Klemke, R. L. PEAK1, a Novel Kinase Target in the Fight Against Cancer.  
872     *Oncotarget* **1**, 219–223 (2010).
- 873 61. Nguyen, T. T. T. *et al.* PLEKHG3 enhances polarized cell migration by activating actin  
874     filaments at the cell front. *Proc. Natl. Acad. Sci. U.S.A.* **113**, 10091–10096 (2016).
- 875 62. Oliver, C. J. *et al.* Targeting Protein Phosphatase 1 (PP1) to the Actin Cytoskeleton: the  
876     Neurabin I/PP1 Complex Regulates Cell Morphology. *Molecular and Cellular Biology* **22**,  
877     4690–4701 (2002).
- 878 63. Barnes, A. P., Smith, F. D., VanDongen, H. M., VanDongen, A. M. J. & Milgram, S. L.  
879     The identification of a second actin-binding region in spinophilin/neurabin II. *Molecular  
880     Brain Research* **124**, 105–113 (2004).
- 881 64. Smith, C. *et al.* Septin 9 Exhibits Polymorphic Binding to F-Actin and Inhibits Myosin and  
882     Cofilin Activity. *Journal of Molecular Biology* **427**, 3273–3284 (2015).
- 883 65. Hildebrand, J. D. & Soriano, P. Shroom, a PDZ Domain–Containing Actin-Binding  
884     Protein, Is Required for Neural Tube Morphogenesis in Mice. *Cell* **99**, 485–497 (1999).
- 885 66. Yeo, N. C. *et al.* Shroom3 contributes to the maintenance of the glomerular filtration  
886     barrier integrity. *Genome Res.* **25**, 57–65 (2015).
- 887 67. Belardi, B. *et al.* A Weak Link with Actin Organizes Tight Junctions to Control Epithelial  
888     Permeability. *Developmental Cell* **54**, 792-804.e7 (2020).
- 889 68. Pacholsky, D. *et al.* Xin repeats define a novel actin-binding motif. *Journal of Cell  
890     Science* **117**, 5257–5268 (2004).
- 891 69. Schulze, J. O. *et al.* Structural and functional characterization of human Iba proteins. *The  
892     FEBS Journal* **275**, 4627–4640 (2008).
- 893 70. Boeynaems, S. *et al.* Aberrant phase separation is a common killing strategy of positively  
894     charged peptides in biology and human disease. Preprint at  
895     <https://doi.org/10.1101/2023.03.09.531820> (2023).
- 896 71. Chrifi, I. *et al.* Cgnl1, an endothelial junction complex protein, regulates GTPase  
897     mediated angiogenesis. *Cardiovascular Research* **113**, 1776–1788 (2017).

- 898 72. Zhao, B.-W. *et al.* FBXO34 Regulates the G2/M Transition and Anaphase Entry in  
899 Meiotic Oocytes. *Front. Cell Dev. Biol.* **9**, 647103 (2021).
- 900 73. Estrada, L. Fgd1, the Cdc42 guanine nucleotide exchange factor responsible for  
901 faciogenital dysplasia, is localized to the subcortical actin cytoskeleton and Golgi  
902 membrane. *Human Molecular Genetics* **10**, 485–495 (2001).
- 903 74. Inokuchi, J. *et al.* Deregulated expression of KRAP, a novel gene encoding actin-  
904 interacting protein, in human colon cancer cells. *J Hum Genet* **49**, 46–52 (2004).
- 905 75. Rivera Alvarez, J. *et al.* The kinesin Kif21b regulates radial migration of cortical projection  
906 neurons through a non-canonical function on actin cytoskeleton. *Cell Reports* **42**, 112744  
907 (2023).
- 908 76. Abé, T. *et al.* Ladinin-1 in actin arcs of oral squamous cell carcinoma is involved in cell  
909 migration and epithelial phenotype. *Sci Rep* **14**, 22778 (2024).
- 910 77. Wong, M. J., Malapitan, I. A., Sikorski, B. A. & Jongstra, J. A cell-free binding assay  
911 maps the LSP1 cytoskeletal binding site to the COOH-terminal 30 amino acids.  
912 *Biochimica et Biophysica Acta (BBA) - Molecular Cell Research* **1642**, 17–24 (2003).
- 913 78. Cervero, P., Wiesner, C., Bouissou, A., Poincloux, R. & Linder, S. Lymphocyte-specific  
914 protein 1 regulates mechanosensory oscillation of podosomes and actin isoform-based  
915 actomyosin symmetry breaking. *Nat Commun* **9**, 515 (2018).
- 916 79. Sandeep, P. *et al.* Neuron navigators: A novel frontier with physiological and pathological  
917 implications. *Molecular and Cellular Neuroscience* **127**, 103905 (2023).
- 918 80. Maas, M. N. *et al.* Examining prestructured  $\beta$ -actin peptides as substrates of histidine  
919 methyltransferase SETD3. *Sci Rep* **14**, 26439 (2024).
- 920 81. Fredriksson-Lidman, K., Van Itallie, C. M., Tietgens, A. J. & Anderson, J. M. Sorbin and  
921 SH3 domain-containing protein 2 (SORBS2) is a component of the acto-myosin ring at  
922 the apical junctional complex in epithelial cells. *PLoS ONE* **12**, e0185448 (2017).
- 923 82. Mehta, V. *et al.* SPECC1L binds the myosin phosphatase complex MYPT1/PP1 $\beta$  and  
924 can regulate its distribution between microtubules and filamentous actin. *Journal of  
925 Biological Chemistry* **299**, 102893 (2023).

- 926 83. Chen, Y. *et al.* F-actin and Myosin II Binding Domains in Supervillin. *Journal of Biological  
927 Chemistry* **278**, 46094–46106 (2003).
- 928 84. Pestonjamasp, K. N., Pope, R. K., Wulfkuhle, J. D. & Luna, E. J. Supervillin (p205): A  
929 Novel Membrane-associated, F-Actin-binding Protein in the Villin/Gelsolin Superfamily.  
930 *The Journal of Cell Biology* **139**, 1255–1269 (1997).
- 931 85. Wulfkuhle, J. D. *et al.* Domain analysis of supervillin, an F-actin bundling plasma  
932 membrane protein with functional nuclear localization signals. *Journal of Cell Science*  
933 **112**, 2125–2136 (1999).
- 934 86. Kadzik, R. S., Homa, K. E. & Kovar, D. R. F-Actin Cytoskeleton Network Self-  
935 Organization Through Competition and Cooperation. *Annu. Rev. Cell Dev. Biol.* **36**, 35–  
936 60 (2020).
- 937 87. Pollard, T. D. Actin and Actin-Binding Proteins. *Cold Spring Harb Perspect Biol* **8**,  
938 a018226 (2016).
- 939 88. Davey, N. E., Cyert, M. S. & Moses, A. M. Short linear motifs – ex nihilo evolution of  
940 protein regulation. *Cell Commun Signal* **13**, 43 (2015).
- 941 89. Van Roey, K. *et al.* Short Linear Motifs: Ubiquitous and Functionally Diverse Protein  
942 Interaction Modules Directing Cell Regulation. *Chem. Rev.* **114**, 6733–6778 (2014).
- 943 90. Weed, S. A. *et al.* Cortactin localization to sites of actin assembly in lamellipodia requires  
944 interactions with F-actin and the Arp2/3 complex. *J Cell Biol* **151**, 29–40 (2000).
- 945 91. Nanda, S. *et al.* Rho GTPase activity crosstalk mediated by Arhgef11 and Arhgef12  
946 coordinates cell protrusion-retraction cycles. *Nat Commun* **14**, 8356 (2023).
- 947 92. Henikoff, S. & Henikoff, J. G. Amino acid substitution matrices from protein blocks. *Proc  
948 Natl Acad Sci U S A* **89**, 10915–10919 (1992).
- 949 93. Altschul, S. Gapped BLAST and PSI-BLAST: a new generation of protein database  
950 search programs. *Nucleic Acids Research* **25**, 3389–3402 (1997).
- 951 94. Steinegger, M. *et al.* HH-suite3 for fast remote homology detection and deep protein  
952 annotation. *BMC Bioinformatics* **20**, 473 (2019).

- 953 95. Mirdita, M. *et al.* ColabFold: making protein folding accessible to all. *Nat Methods* **19**,  
954 679–682 (2022).
- 955 96. Crooks, G. E., Hon, G., Chandonia, J.-M. & Brenner, S. E. WebLogo: A Sequence Logo  
956 Generator: Figure 1. *Genome Res.* **14**, 1188–1190 (2004).
- 957 97. Li, M. Z. & Elledge, S. J. SLIC: A Method for Sequence- and Ligation-Independent  
958 Cloning. in *Gene Synthesis* (ed. Peccoud, J.) vol. 852 51–59 (Humana Press, Totowa,  
959 NJ, 2012).
- 960 98. Pardee, J. D. & Aspudich, J. [18] Purification of muscle actin. in *Methods in Enzymology*  
961 vol. 85 164–181 (Elsevier, 1982).
- 962 99. Kimanis, D., Dong, L., Sharov, G., Nakane, T. & Scheres, S. H. W. New tools for  
963 automated cryo-EM single-particle analysis in RELION-4.0. *Biochemical Journal* **478**,  
964 4169–4185 (2021).
- 965 100. Zheng, S. Q. *et al.* MotionCor2: anisotropic correction of beam-induced motion for  
966 improved cryo-electron microscopy. *Nat Methods* **14**, 331–332 (2017).
- 967 101. Rohou, A. & Grigorieff, N. CTFFIND4: Fast and accurate defocus estimation from  
968 electron micrographs. *Journal of Structural Biology* **192**, 216–221 (2015).
- 969 102. Wagner, T. *et al.* SPHIRE-crYOLO is a fast and accurate fully automated particle  
970 picker for cryo-EM. *Commun Biol* **2**, 218 (2019).
- 971 103. Pospich, S., Merino, F. & Raunser, S. Structural Effects and Functional Implications of  
972 Phalloidin and Jasplakinolide Binding to Actin Filaments. *Structure* **28**, 437-449.e5  
973 (2020).
- 974 104. Goddard, T. D. *et al.* UCSF ChimeraX: Meeting modern challenges in visualization  
975 and analysis. *Protein Science* **27**, 14–25 (2018).
- 976 105. Croll, T. I. /SOLDE: a physically realistic environment for model building into low-  
977 resolution electron-density maps. *Acta Crystallogr D Struct Biol* **74**, 519–530 (2018).
- 978 106. Afonine, P. V. *et al.* Real-space refinement in PHENIX for cryo-EM and  
979 crystallography. *Acta Crystallogr D Struct Biol* **74**, 531–544 (2018).

- 980 107. Herzog, R., Van Den Dries, K., Cervero, P. & Linder, S. Poji: a Fiji-based tool for  
981 analysis of podosomes and associated proteins. *Journal of Cell Science* **133**, jcs238964  
982 (2020).
- 983 108. Belyy, A. *et al.* Actin activates *Pseudomonas aeruginosa* ExoY nucleotidyl cyclase  
984 toxin and ExoY-like effector domains from MARTX toxins. *Nat Commun* **7**, 13582 (2016).
- 985 109. Schneider, C. A., Rasband, W. S. & Eliceiri, K. W. NIH Image to ImageJ: 25 years of  
986 image analysis. *Nat Methods* **9**, 671–675 (2012).
- 987 110. Paraschiakos, T. Position Specific Frequency Matrix v1.0. Zenodo  
988 <https://doi.org/10.5281/ZENODO.10702806> (2024).
- 989 111. Zdobnov, E. M. *et al.* OrthoDB in 2020: evolutionary and functional annotations of  
990 orthologs. *Nucleic Acids Research* **49**, D389–D393 (2021).
- 991 112. Wright, E. S. DECIPHER: harnessing local sequence context to improve protein  
992 multiple sequence alignment. *BMC Bioinformatics* **16**, 322 (2015).
- 993 113. Minh, B. Q. *et al.* IQ-TREE 2: New Models and Efficient Methods for Phylogenetic  
994 Inference in the Genomic Era. *Molecular Biology and Evolution* **37**, 1530–1534 (2020).
- 995 114. Löytynoja, A. Phylogeny-aware alignment with PRANK. in *Multiple Sequence  
996 Alignment Methods* (ed. Russell, D. J.) vol. 1079 155–170 (Humana Press, Totowa, NJ,  
997 2014).
- 998 115. Pond, S. L. K., Frost, S. D. W. & Muse, S. V. HyPhy: hypothesis testing using  
999 phylogenies. *Bioinformatics* **21**, 676–679 (2005).
- 1000 116. Ge, S. X., Jung, D. & Yao, R. ShinyGO: a graphical gene-set enrichment tool for  
1001 animals and plants. *Bioinformatics* **36**, 2628–2629 (2020).
- 1002
- 1003
- 1004
- 1005
- 1006
- 1007

1008 **Figure Legends**

1009 **Figure 1: Structural alignment of ITPKA<sup>Arg28-Ala49</sup> and Lifeact points towards a novel F-**  
1010 **actin binding motif, prompting proteome-wide discovery using the SLiMFold pipeline.**  
1011 **(a)** Structural superimposition of the ITPKA<sup>Arg28-Ala49</sup>–actin complex (orange and red for the two  
1012 actin subunits, cyan for ITPKA) with the Lifeact–actin structure (grey; PDB: 7AD9) shows near-  
1013 identical actin conformations apart from a minor shift in the D-loop of the ITPKA-bound model.  
1014 **(b)** Rotating the helices by 180° highlights the residues interacting with F-actin. Conserved  
1015 side chains are represented as sticks and labeled P1, P4, P8, and P9. **(c)** Domain architecture  
1016 of *S. cerevisiae* ABP140 and *H. sapiens* ITPKA. ABP140 comprises an N-terminal F-actin  
1017 binding domain (ABD) and a C-terminal methyltransferase (MTase) domain. ITPKA features  
1018 an N-terminal ABD, a central calmodulin-binding domain (CaMBD), and a C-terminal inositol  
1019 1,4,5-trisphosphate 3-kinase (IP3K) domain. Notably, the F-actin binding motifs, derived in this  
1020 study, are located within intrinsically disordered regions, which is typical for short linear motifs  
1021 (SLiMs). **(d)** Sequence comparison underscores structural and sequence conservation,  
1022 conserved positions P1, P4, P8, and P9 are labeled in red. **(e)** SLiMFold pipeline overview.  
1023 The SLiMFold pipeline started with the hypothesized SLiMs of Lifeact and ITPKA<sup>Arg28-Ala49</sup>  
1024 Sequence, on which basis a position-specific scoring matrix (PSSM) was calculated to identify  
1025 motif hits from NCBI databases which were filtered by PSSM scores, IUPRED, ANCHOR, and  
1026 PSIPRED. This yielded 539 hits in the first iteration. Thereafter, multiple sequence alignments  
1027 (MSAs) were calculated locally using UniRef90 with modified jackhmmer filters, followed by  
1028 multimer predictions on ColabFold. The predicted structures were analyzed by extracting  
1029 AlphaFold2 scores, computing RMSD and angle metrics ( $\theta$ ,  $\varphi$ ). These data were clustered to  
1030 identify 59 new sequences that carry the suspected motif. **(f-i)** Detailed illustration of calculated  
1031 metadata from (e). **(f)** Scatterplot of predicted peptide–actin complexes plotting mean ipTM vs.  
1032 RMSD relative to ITPKA<sup>Arg28-Ala49</sup>. A red dotted line at ipTM=0.6 marks the threshold below  
1033 which interactions are unreliable. **(g)** Helix orientation was assessed by comparing  $\Delta\varphi$  and  $\Delta\theta$   
1034 angles in a polar coordinate system after superimposing each complex onto the ITPKA<sup>Arg28-</sup>  
1035 <sup>Ala49</sup>–actin reference. **(h)** A 3D plot of  $\Delta\varphi$ ,  $\Delta\theta$ , and helix polarity (1 = same direction, -1 =  
1036 opposite) maps each predicted peptide, with data points colored by  $\log(1+\text{RMSD})$ . Angles near  
1037 zero indicate an orientation similar to that of ITPKA<sup>Arg28-Ala49</sup>. **(i)** HDBSCAN clustering of these  
1038 data points groups peptides based on orientation and RMSD. Outliers are assigned to Cluster  
1039 -1, while Cluster 3 contains helices most closely matching ITPKA<sup>Arg28-Ala49</sup>. **(j)** Sequence logo  
1040 depicting positional conservation among the 59 identified peptides confirms robust  
1041 conservation at positions P1, P4, P8, and P9, strongest at P1 and P8.

1042

1043 **Figure 2: Validation and functional analysis of the novel short linear F-actin binding**  
1044 **motif (SFM) by cellular F-actin colocalization.** **(a)** Five peptides identified by the SLiMFold  
1045 pipeline were aligned with the sequences of ITPKA and Lifeact; the conserved positions P1,  
1046 P4, P8, P9 are highlighted in red. To probe their functional significance, the peptides were  
1047 cloned into an pEGFP vector, and alanine mutations were introduced at P1 and P8. **(b)** Primary  
1048 human macrophages were transfected with the vectors coding for the EGFP-tagged peptides  
1049 and stained with phalloidin-568 to visualize F-actin (red). Representative cell images are  
1050 shown including zoomed- into one podosome substructure, scale bars: 10 and 5  $\mu\text{m}$ ,  
1051 respectively. Colocalization is evident when EGFP-tagged peptides (green) overlap with  
1052 phalloidin-stained actin (red). Right panels: Imaris 3D reconstructions and Poji radial profiles  
1053 confirm varying degrees of peptide–actin colocalization. Shown are Poji radial profiles of  
1054 fluorescence intensities, at a z plane of highest F-actin intensity, with the mean values of F-  
1055 actin and respective peptide  $\pm$  standard deviation of at least 3 cells, and 240 podosomes per  
1056 transfected peptide. Poji radial profiles were normalized to set the intensity values from 0% to  
1057 100%.

1058

1059 **Figure 3: Determination of SFM-binding affinities to F-actin, and identification of affinity-**  
1060 **modulating amino acids.** (a) Six further peptides identified by the SLiMFold pipeline were  
1061 aligned with the sequences of ITPKA and Lifeact, and the conserved positions P1, P4, P8, and  
1062 P9 highlighting in red. The peptides were expressed in bacteria, and after purification F-actin  
1063 pull-downs were performed. Binding of the peptides were analyzed by Western blotting, and  
1064 to calculate relative dissociation constants ( $K_D$  values), the F-actin concentrations were plotted  
1065 against normalized band intensities. The right panel provides the  $K_D$ -values for all peptides  
1066 tested. (c) In order to identify the amino acids modulating the affinity of the peptides to F-actin,  
1067 their frequency was analyzed by generating a position specific matrix (PSFM) using MSA from  
1068 CEFIP, USP54, ITPKA, PPP1R9A, Lifeact, ARHGEF11, FGD4, DIXDC1. Y-axis represents  
1069 positively charged (+), negatively charged (-), polar (P), unique (U), non-polar (NP) and  
1070 aromatic (A) residues, and X-axis the position inside the SFM. This matrix, color-coded by  
1071  $\sqrt{(\text{amino acid frequency})}$ , pinpointed less (white) and more frequent (red) residues. (d)  
1072 SHROOM3 and USP54 wild-type (WT) sequences and corresponding mutants, including the  
1073 key residues P1, P4, P8, P9. M2 features mutations N-terminal to the motif, M3 contains  
1074 mutations within the motif, and M4 includes mutations C-terminal to the motif. M1 incorporates  
1075 all mutations (N-terminal, within, and C-terminal). Newly mutated positions are labeled in red.  
1076 (e) Quantified relative band intensities from SHROOM3 and USP54 pulldown assays,  
1077 normalized and averaged across replicates, highlighting differences in binding affinities  
1078 between WT and mutant peptides. (f) For USP54 M1 addiotinally the affinity to F-actin was  
1079 determined. Statistical significance is denoted by asterisks: \* $p < 0.05$ ; \*\* $p < 0.01$ .

1080

1081 **Figure 4: Evolutionary analysis of validated SFM-containing proteins.** (a) Sequence logos  
1082 of SFMs from representative organism classes (e.g., *Actinopteri*, *Coelacanthiformes*,  
1083 *Amphibia*, *Mammalia*, *Lepidosauria*, *Testudines*, *Aves*, and *Crocodylia*). Key motif positions  
1084 P1, P4, P8, and P9 are labeled. Larger letters indicate higher residue conservation, reinforcing  
1085 the importance of these positions for F-actin binding. (b) A dN/dS ratio analysis of all validated  
1086 SFM-containing peptides is plotted  $\pm$  SEM, with amino acid position on the x-axis and the  
1087 dN/dS ratio on the y-axis. The conserved SFM residues (P1, P4, P8, P9) are annotated to  
1088 highlight their selective pressures. Notably, these positions exhibit lower dN/dS values,  
1089 suggesting strong purifying selection. (c) Phylogenetic tree illustrating the distribution of  
1090 validated SFM-containing proteins across various species. Symbols mark the most recent  
1091 common ancestor (MRCA) *Saccharomyces* (ABP140), *Bilateria* (SHROOM3), *Vertebrata*  
1092 (CGNL1, DIXDC1, FGD4, PPP1R9A), *Euteleostomi* (ARHGEF11, ITPKA), and  
1093 *Gnathostomata* (CEFI, DENND1C, ESPLN, FGD1, FGD4, USP54).

1094

1095 **Figure 5: Iterative SLiMFold pipeline expansion and functional classification of newly**  
1096 **identified SFM-containing proteins.** (a) Scheme of three iterative SLiMFold rounds (for  
1097 detailed description, see Figure 3), including *in vitro* and *in cellulo* validation, yielding 124  
1098 peptide-sequences from 103 different genes. (b) Cartoon representation of a eukaryotic cell  
1099 highlighting the functional categories of new SFM-bearing proteins. SFM candidates are  
1100 grouped according to their principal roles and subcellular localizations, encompassing direct  
1101 actin modulators, actin regulators, other signaling proteins and enzymes, nuclear structure and  
1102 RNA processing, chromatin modification and DNA repair, microtubule-associated factors, cilia,  
1103 and cell-junction-associated proteins. Proteins for which F-actin binding has been attributed to  
1104 the SFM (e.g., validated by truncation studies) are marked with an asterisk (\*), whereas  
1105 proteins that bind F-actin but lack direct evidence linking the interaction specifically to the SFM  
1106 are marked with a dagger (†). The cartoon was created with BioRender.com.

| Gene      | Protein name                                       | Uniprot ID | Start | End  | Sequence   | ipTM | Iteration | Comment   |
|-----------|--|------------|-------|------|------------|------|-----------|---|
| ABRA      | actin-binding Rho-activating protein               | Q8N0Z2     | 242   | 250  | VGNLKGRWQ  | 0.86 | 1         | In line with our motif, F-actin binding shown by STARS [ABRA] by two regions AA 234–279 and AA 346–375. <sup>1</sup>                          |
| AIF1L     | allograft inflammatory factor 1-like               | Q9BQI0     | 119   | 127  | VLKLVMMFE  | 0.78 | 2         | No specific domain/motif analyzed, but F-Actin binding shown. <sup>2</sup>  |
| ANK2      | ankyrin-2  | Q01484     | 1990  | 1998 | VRELMKAFQ  | 0.90 | 1         |   |
| ANK3      | ankyrin-3  | Q12955     | 2715  | 2723 | LSSIRLKFE  | 0.64 | 3         |   |
| ANKLE1    | ankyrin repeat and LEM domain-containing protein 2 | Q86XL3     | 729   | 737  | VSDLTVEFD  | 0.84 | 3         |   |
| ANKRD55   | ankyrin repeat domain-containing protein 55        | Q3KP44     | 378   | 386  | VNDIITTFD  | 0.68 | 3         |   |
| ARHGAP11A | rho GTPase-activating protein 11A                  | Q6P4F7     | 808   | 816  | VSDHIQWFN  | 0.84 | 3         |   |
| ARHGAP42  | rho GTPase-activating protein 42                   | A6NI28     | 799   | 807  | VAAKAQLFE  | 0.84 | 2         |   |
| ARHGEF11  | rho guanine nucleotide exchange factor 11          | O15085     | 565   | 573  | VRNIIQHFE  | 0.90 | 1         | Validates our motif, F-actin binding shown by ARHGEF11 through AA 561–585. <sup>3</sup>   |
| ARHGEF15  | rho guanine nucleotide exchange factor 15          | O94989     | 150   | 158  | VRRLAGRFE  | 0.84 | 1         |   |
| BCR       | breakpoint cluster region protein                  | P11274     | 151   | 159  | VAALRSNFE  | 0.85 | 1         |   |
| BRD10     | uncharacterized bromodomain-containing protein 10  | Q5HYC2     | 773   | 781  | LRELITKIE  | 0.72 | 3         |   |
| CEFIP     | cardiac-enriched FHL2-interacting protein          | Q711Q0     | 143   | 151  | VSTLIKSFD  | 0.89 | 1         |   |
| C4orf54   | uncharacterized protein C4orf54                    | D6RIA3     | 1352  | 1360 | VSARAAAFAE | 0.78 | 2         | No specific domain/motif analyzed, but F-Actin binding shown. <sup>4</sup>  |
| C6orf132  | uncharacterized protein C6orf132                   | Q5T0Z8     | 563   | 571  | VRQIRNELE  | 0.81 | 3         |   |
| C9orf152  | uncharacterized protein C9orf152                   | Q5JTZ5     | 39    | 47   | IQFLRAQYE  | 0.63 | 3         |   |
| CALD1     | caldesmon  | Q05682     | 709   | 716  | VRNIKSMWE  | 0.85 | 3         | Validates our motif, F-actin binding shown by Gallus CALD1 through AA 666–683. In Gallus CALD1 our Motif corresponds to 667–675. <sup>5</sup> |
| CAMSAP2   | calmodulin-regulated spectrin-associated protein 2 | Q08AD1     | 845   | 853  | LADIKESME  | 0.72 | 3         |   |
| CASKIN1   | caskin-1   | Q8WXD9     | 1001  | 1009 | VKSIAAMLE  | 0.90 | 3         |   |
| CCDC14    | coiled-coil domain-containing protein 14           | Q49A88     | 453   | 461  | IQLRLITEME | 0.73 | 3         |   |
| CCDC150   | coiled-coil domain-containing protein 150          | Q8NCX0     | 828   | 836  | IEALRKQFQ  | 0.82 | 3         |   |
| CGN       | cingulin   | Q9P2M7     | 178   | 186  | VDSLINKFD  | 0.90 | 1         | Validates our motif, F-actin binding shown by Xenopus CGN through AA 101–294. In Xenopus CGN our Motif corresponds to 267–275. <sup>6</sup>   |
| CGNL1     | cingulin-like protein 1                            | Q0VF96     | 353   | 361  | VDQLIEKFD  | 0.89 | 1         | No specific domain/motif analyzed, but F-Actin binding shown. <sup>7</sup>  |

|         |  |            |      |      |           |      |   |  |
|---------|--|------------|------|------|-----------|------|---|--|
| CTTN    | src substrate cortactin                          | Q14247     | 347  | 355  | TSNIRANFE | 0.76 | 1 | Validates our motif, F-actin binding shown by CTTN by "helical domain".<br>Corresponds approx. to AA 348-401. <sup>8</sup> |
| CRYBG3  | very large A-kinase anchor protein               | Q68DQ2     | 2045 | 2053 | RTDLVHHFE | 0.74 | 3 |  |
| DBNDD2  | dysbindin domain-containing protein 2            | Q9BQY9     | 114  | 122  | LRERQKFFE | 0.78 | 3 |  |
| DENND1A | DENN domain-containing protein 1A                | Q8TEH3     | 998  | 1006 | VEQLRKQWE | 0.76 | 1 |  |
| DENND1C | DENN domain-containing protein 1C                | Q8IV53     | 792  | 800  | VADLKKCFE | 0.76 | 1 | Validates our motif, F-actin binding shown by DENND1C through AA 786-801. <sup>9</sup>                                     |
| DENND2C | DENN domain-containing protein 2C                | Q68D51     | 21   | 29   | IKQKISQWE | 0.87 | 3 |  |
| DIXDC1  | dixin  | Q155Q3     | 198  | 206  | VRALVQQYE | 0.88 | 1 | Validates our motif, F-actin binding shown by DIXDC1 through AA 127-300. <sup>10</sup>                                     |
| DSP     | desmoplakin                                      | P15924     | 1203 | 1211 | MSNLRNKYE | 0.77 | 1 |  |
| DZIP1L  | cilium assembly protein DZIP1L                   | Q8IYY4     | 671  | 679  | VQSMVKNLE | 0.84 | 2 |  |
| EML1    | echinoderm microtubule-associated protein-like 1 | O00423     | 33   | 41   | VTDRIASLE | 0.74 | 3 |  |
| ENKD1   | enkurin domain-containing protein 1              | Q9H0I2     | 74   | 82   | VGDVLLQLE | 0.72 | 1 |  |
| ESPN    | espin isoform                                    | A0A1B0GUN9 | 949  | 957  | VQHLRATYE | 0.88 | 2 |  |
| ESPNL   | espin-like protein                               | Q6ZVH7     | 652  | 660  | VRTLRGNF  | 0.87 | 1 |  |
| FBXO34  | F-box only protein 34                            | Q9NWN3     | 279  | 287  | VLDMVAKLE | 0.87 | 1 | No specific domain/motif analyzed, but F-Actin colocalization shown. <sup>11</sup>   |
| FGD1    | FYVE, RhoGEF and PH domain-containing protein 1  | P98174     | 211  | 219  | VSSLIEKFE | 0.89 | 1 | No specific domain/motif analyzed, but F-Actin colocalization shown. <sup>12</sup>   |
| FGD2    | FYVE, RhoGEF and PH domain-containing protein 2  | Q7Z6J4     | 12   | 20   | VSNLVTVFE | 0.87 | 1 |  |
| FGD4    | FYVE, RhoGEF and PH domain-containing protein 4  | Q96M96     | 20   | 28   | VSDLISRFE | 0.84 | 1 | Validates our motif, F-actin binding shown by FGD4 through AA 23-28. <sup>3</sup>  |
| FHOD3   | FH1/FH2 domain-containing protein 3              | Q2V2M9     | 745  | 753  | VKAFAEKFN | 0.67 | 3 |  |
| FYB2    | FYN-binding protein 2                            | Q5VWT5     | 9    | 17   | FKELRAKFQ | 0.63 | 1 |  |
| HCLS1   | hematopoietic lineage cell-specific protein      | P14317     | 235  | 243  | TRGLKAKFE | 0.71 | 1 | Validates our motif, F-actin binding shown by HCLS1 by "Coiled-coil domain".<br>Corresponds to AA 215-280. <sup>13</sup>   |
| HOOK1   | protein Hook homolog 1                           | Q9UJC3     | 517  | 525  | IRELQQQIE | 0.61 | 3 |  |
| IER5    | immediate early response gene 5 protein          | Q5VY09     | 266  | 274  | VANLISIFG | 0.78 | 1 |  |
| IL16    | pro-interleukin-16                               | Q14005     | 839  | 847  | IRQRISSFE | 0.76 | 2 |  |
| ITPKA   | inositol-trisphosphate 3-kinase A                | P23677     | 31   | 39   | VGELRLLFE | 0.87 | 1 | Validates our motif, F-actin binding shown by ITPKA through AA 9-52. <sup>14</sup>   |
| ITPKB   | inositol-trisphosphate 3-kinase B                | P27987     | 143  | 151  | VNQKVGMFE | 0.74 | 2 | Validates our motif, F-actin binding shown by ITPKB through AA 108-170. <sup>15</sup>                                      |
| ITPRID2 | protein ITPRID2                                  | P28290     | 169  | 177  | VSELLELYE | 0.74 | 2 | No specific domain/motif analyzed, but F-Actin colocalization shown. <sup>16</sup>   |

|         |  |        |      |      |           |      |   |  |
|---------|--|--------|------|------|-----------|------|---|--|
| KIF21B  | kinesin-like protein KIF21B                                      | O75037 | 866  | 874  | VSSIVRQWN | 0.90 | 1 | No specific domain/motif analyzed, but F-Actin colocalization shown. <sup>17</sup>   |
| KIF23   | kinesin-like protein KIF23                                       | Q02241 | 722  | 730  | VASCISEWE | 0.84 | 3 |  |
| LAD1    | ladinin-1  | O00515 | 438  | 446  | VASKRHLFE | 0.78 | 1 | No specific domain/motif analyzed, but F-Actin colocalization shown. <sup>18</sup>   |
| LCA5    | lebercillin  | Q86VQ0 | 258  | 266  | LAERKRAYE | 0.66 | 3 |  |
| LETM1   | mitochondrial proton/calcium exchanger protein precursor         | O95202 | 612  | 620  | VQQMIGQID | 0.73 | 2 |  |
| LIMA1   | LIM domain and actin-binding protein 1                           | Q9UHB6 | 194  | 202  | LNRLKMMFE | 0.82 | 1 | In line with our motif, F-actin binding shown by LIMA1 by two regions, of which one is located N-terminally (AA 1-260). <sup>19</sup>  |
| LSP1    | lymphocyte-specific protein 1                                    | P33241 | 260  | 268  | VASTKSRWE | 0.85 | 3 | Our motif was not analyzed, but F-Actin colocalization shown by other actin binding domains (Caldesmon like binding domain and villin headpiece like binding domain). <sup>20,21</sup> |
| METTL25 | probable methyltransferase-like protein 25                       | Q8N6Q8 | 286  | 294  | ISNIRNQME | 0.65 | 2 |  |
| MTUS2   | microtubule-associated tumor suppressor candidate 2              | Q5JR59 | 506  | 514  | VAENRNLL  | 0.71 | 1 |  |
| MYO15B  | myosin XVB   | Q96JP2 | 2147 | 2155 | IGNIIRMYQ | 0.61 | 1 |  |
| MYO18A  | unconventional myosin-XVIIa                                      | Q92614 | 1685 | 1693 | IAQLKNQLE | 0.69 | 1 |  |
| N4BP1   | NEDD4-binding protein 1  | O75113 | 244  | 252  | VSELTQKMD | 0.80 | 1 |  |
| NAV2    | neuron navigator 2   | Q8IVL1 | 753  | 761  | IADLRQNLE | 0.67 | 1 | No specific domain/motif analyzed, but F-Actin binding shown. <sup>22</sup>  |
| NAV3    | neuron navigator 3   | Q8IVL0 | 689  | 697  | IADLRQNLE | 0.71 | 1 | No specific domain/motif analyzed, but F-Actin binding shown. <sup>22</sup>  |
| NIN     | ninein   | Q8N4C6 | 755  | 763  | VRGLTQELE | 0.86 | 3 |  |
| OPHN1   | oligophrenin-1   | O60890 | 776  | 784  | VASRTRFFE | 0.87 | 2 | Validates our motif, F-actin binding shown by Oligophrenin through AA 677-802. <sup>23</sup>   |
| PCDH15  | protocadherin-15   | Q96QU1 | 1724 | 1731 | IETERNIFE | 0.64 | 3 |  |
| PDZD2   | PDZ domain-containing protein 2                                  | O15018 | 2335 | 2343 | VKQRIKSFE | 0.85 | 2 |  |
| PEAK1   | inactive tyrosine-protein kinase PEAK1                           | Q9H792 | 702  | 710  | VAQKVQEFN | 0.79 | 3 | Validates our motif, F-actin binding shown by inactive tyrosine-protein kinase PEAK1 through AA 339-727. <sup>24</sup>   |
| PHC2    | polyhomeotic-like protein 2                                      | Q8IXK0 | 594  | 602  | VGNLKKKYA | 0.68 | 1 |  |
| PLCB2   | 1-phosphatidylinositol 4,5-bisphosphate phosphodiesterase beta-2 | Q00722 | 1040 | 1048 | TKEMKKKLE | 0.75 | 3 |  |
| PLEKHD1 | pleckstrin homology domain-containing family D member 1          | A6NEE1 | 396  | 404  | VSHLKRFTE | 0.83 | 2 |  |
| PLEKHG2 | pleckstrin homology domain-containing family G member 2          | Q9H7P9 | 817  | 825  | VRELARLYS | 0.83 | 2 |  |
| PLEKHG3 | pleckstrin homology domain-containing                            | A1L390 | 1205 | 1213 | VRNLREKFQ | 0.74 | 1 |  |

|         |  |           |      |      |            |      |   |   |
|---------|--|-----------|------|------|------------|------|---|---|
|         | family G member 3  |           | 926  | 934  | VYQLARQYS  | 0.84 | 3 |   |
|         |  |           | 750  | 758  | VRNSISRNF  | 0.87 | 3 | Validates our motif. F-actin binding suggested for AA 910 to 940. The others could not be found due to limited truncation design; By elongating the N terminus from 1 to 910 (instead of 1- to 600), one could have possibly still observed an actin binding (probably mediated by region 750 - 758). The same accounts for the C terminal truncations, where a construct from 940 - 1219 would also probably still show actin binding (instead of 940 - 1100). <sup>25</sup> |
| PPP1R9A | neurabin-1   | Q9ULJ8    | 139  | 147  | FTETRKMF   | 0.88 | 1 |   |
|         |  |           | 202  | 210  | VSQLSAVFE  | 0.87 | 1 | Validates our motif, F-actin binding shown by Neurabin-1 through AA 1-144. <sup>26</sup>  |
|         |  |           | 120  | 128  | VSERISRFD  | 0.85 | 1 |   |
| PPP1R9B | neurabin-2   | Q96SB3    | 144  | 152  | LQETRKLF   | 0.62 | 1 |   |
|         |  |           | 208  | 216  | VSQLSAVFE  | 0.88 | 1 | Validates our motif, F-actin binding shown by Neurabin-2 through 2 regions, AA 1-154 and AA 151-282. <sup>27</sup>  |
| PPRC1   | peroxisome proliferator-activated receptor gamma coactivator-related protein 1 | Q5VV67    | 1172 | 1180 | LSSLLEQFE  | 0.60 | 1 |   |
| PXN     | paxillin   | P49023    | 217  | 225  | VESLLDELE  | 0.79 | 3 |   |
| RAMAC   | RNA guanine-N7 methyltransferase activating subunit                            | Q9BTL3    | 4    | 12   | TAEAVPKFE  | 0.85 | 1 |   |
| RAPH1   | ras-associated and pleckstrin homology domains-containing protein 1            | Q70E73    | 862  | 870  | VKQIASHQFP | 0.72 | 3 |   |
| RCSD1   | capZ-interacting protein   | Q6JBY9    | 20   | 28   | VAQLAGRFR  | 0.84 | 1 |   |
| ROCK1   | rho-associated protein kinase 1  | Q13464    | 769  | 777  | VKNLTLQLE  | 0.70 | 3 |   |
| SEPTIN9 | septin-9 isoform 7   | Q9UHD8-7  | 5    | 13   | YSALKRSFE  | 0.60 | 1 | Validates our motif, F-actin binding shown by Septin-9 through AA 1-143. <sup>28</sup>  |
| SETD2   | histone-lysine N-methyltransferase SETD2                                       | Q9BYW2    | 2118 | 2126 | TEERRKLFE  | 0.79 | 1 | No binding shown, but methylates actin. <sup>29</sup>   |
| SH2D4B  | SH2 domain-containing protein 4B   | Q5SQS7    | 247  | 255  | VAGLSSMFR  | 0.87 | 1 |   |
| SH2D7   | SH2 domain-containing protein 7  | A6NKC9    | 119  | 127  | LAEVHHYQ   | 0.63 | 3 |   |
| SHROOM3 | protein Shroom3  | Q8TF72    | 781  | 789  | VLEKVKF    | 0.86 | 1 | In line with our motif, F-actin binding shown by Shroom3 throughout the ASD1 region, which incorporated one part of our identified motif (AA 1054 - 1062). <sup>30,31</sup>   |
|         |  |           | 1054 | 1062 | VADRRRLFE  | 0.84 | 1 |   |
| SORBS1  | sorbin and SH3 domain-containing protein 1 isoform 26                          | Q9BX66-12 | 657  | 665  | VRDLASHFE  | 0.85 | 2 |   |
|         |  |           | 691  | 699  | VSSRITAFE  | 0.87 | 1 |   |
| SORBS2  | sorbin and SH3 domain-containing protein 2                                     | O94875    | 473  | 481  | VKSRLQYE   | 0.87 | 3 |   |
|         |  |           | 506  | 514  | VPTRISEFE  | 0.89 | 3 | No specific domain/motif analyzed, but F-Actin colocalization shown. <sup>32</sup>  |

|         |   |        |      |      |                  |      |   |  |
|---------|---|--------|------|------|------------------|------|---|--|
| SPECC1  | cytospin-B  | Q5M775 | 820  | 828  | VKSЛИKSFD        | 0.86 | 1 | F-Actin colocalization shown, but thought to be mediated over other motifs (WH2). <sup>33</sup>  |
| SPECC1L | cytospin-A  | Q69YQ0 | 841  | 849  | VKTLIKSFD        | 0.89 | 1 | F-Actin colocalization shown, but thought to be mediated over other motifs (WH2). <sup>33</sup>  |
| SPEG    | striated muscle preferentially expressed protein kinase | Q15772 | 400  | 408  | ILDKLQFFE        | 0.76 | 1 |  |
|         |   |        | 866  | 874  | VRRATLEFE        | 0.83 | 3 |  |
| SSH2    | protein phosphatase Slingshot homolog 2                 | Q76I76 | 749  | 757  | VKEIVTEIE        | 0.83 | 3 | No specific domain/motif analyzed, but F-Actin binding shown. <sup>34</sup>  |
| SSH3    | protein phosphatase Slingshot homolog 3                 | Q8TE77 | 612  | 620  | VANRTQAFQ        | 0.68 | 2 | No specific domain/motif analyzed, but F-Actin binding shown. <sup>34</sup>  |
| STRN    | striatin  | O43815 | 329  | 337  | ITKLKEQYK        | 0.82 | 3 |  |
| SVIL    | supervillin   | O95425 | 594  | 602  | VAQLRSAFL        | 0.69 | 1 | F-Actin colocalization shown, but thought to be mediated over other domains. <sup>35-37</sup>  |
| SYCP1   | synaptonemal complex protein 1                          | Q15431 | 218  | 226  | IEKMITAFE        | 0.70 | 2 |  |
| TET3    | methylcytosine dioxygenase TET3                         | Q8BG87 | 715  | 723  | LEELIRQFE        | 0.75 | 1 |  |
| TIAM2   | rho guanine nucleotide exchange factor TIAM2            | Q8IVF5 | 296  | 304  | LSSLRELYK        | 0.70 | 3 |  |
| TJP1    | tight junction protein ZO-1                             | Q07157 | 1264 | 1272 | VLTRVKMFE        | 0.90 | 3 | Validates our motif, F-actin binding shown by tight junction protein ZO-1 through AA 1257-1284. <sup>38</sup>  |
| TPRN    | taperin   | Q4KMQ1 | 133  | 141  | VSRLLERFD        | 0.72 | 1 |  |
| USP54   | ubiquitin carboxyl-terminal hydrolase 54                | Q70EL1 | 1129 | 1137 | VRSLAEQFQ        | 0.88 | 1 |  |
|         |   |        | 693  | 701  | VSRQKEVFQ        | 0.82 | 3 |  |
|         |   |        | 123  | 131  | VQATSRKFE        | 0.88 | 2 |  |
|         |   |        | 91   | 99   | VQCMRWIFE        | 0.86 | 3 |  |
|         |   |        | 342  | 350  | VQQQQHLFE        | 0.79 | 1 |  |
| XIRP1   | xin actin-binding repeat-containing protein 1           | Q702N8 | 438  | 446  | <b>VKTFKNLFE</b> | 0.87 | 2 |  |
|         |   |        | 1491 | 1499 | <b>VQALRRLFE</b> | 0.79 | 3 | Validates our motif: defined in this study as a novel, repetitive actin-binding motif present in at least two different muscle proteins. <sup>39</sup> |
|         |   |        | 547  | 555  | VGTARWLFE        | 0.85 | 1 |  |
|         |   |        | 153  | 161  | <b>VRAARWLFE</b> | 0.85 | 3 |  |
|         |   |        | 591  | 599  | VQTIRWLFE        | 0.89 | 1 |  |
| XIRP2   | xin actin-binding repeat-containing protein 2           | A4UGR9 | 399  | 407  | <b>VQSIRWIFE</b> | 0.88 | 2 |  |

|       |   |        |      |                  |                  |      |
|-------|---|--------|------|------------------|------------------|------|
|       |   | 1243   | 1251 | <b>VKTSRQFFE</b> | 0.87             | 3    |
|       |   | 187    | 195  | <b>TKLLKEQFE</b> | 0.82             | 3    |
|       |   | 364    | 372  | <b>VQQARYVFE</b> | 0.79             | 3    |
| XIRP2 | xin actin-binding repeat-containing protein 2 isoform 4 | A4UGR9 | 114  | 122              | <b>LDELRSVFE</b> | 0.78 |

**Table 1. Proteins identified by the SLiMFold pipeline as containing the short linear F-actin-binding motif (SFM).** Each entry includes the gene symbol, protein name, UniProt ID, motif boundaries (Start–End), SFM sequence, the mean ipTM (averaged from the top three SLiMFold models), the SLiMFold iteration in which it was identified, and a brief comment providing functional insight or references.

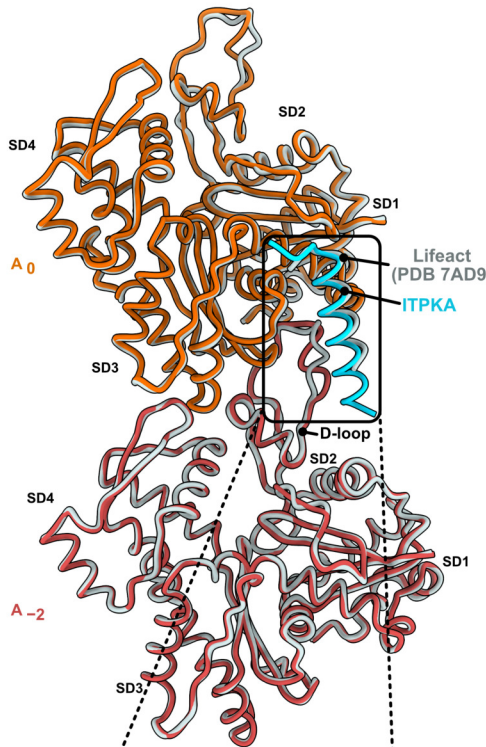
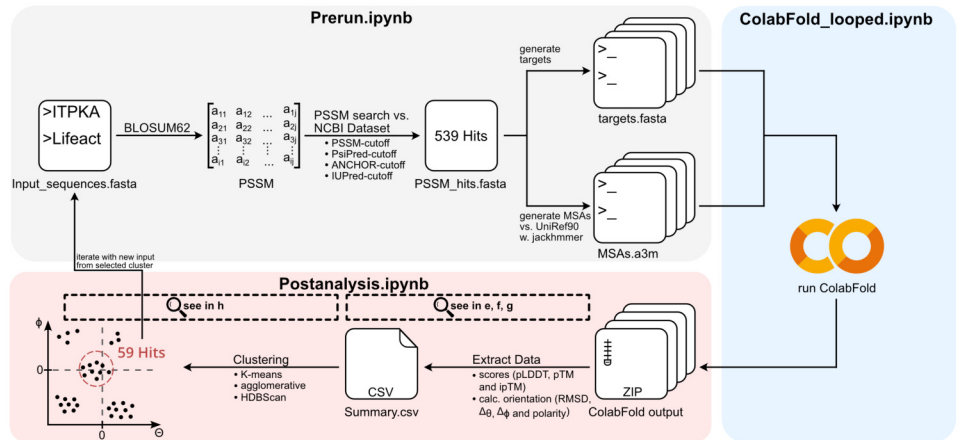
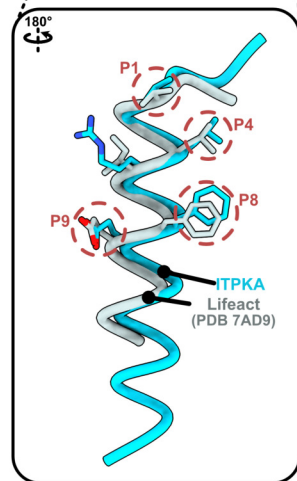
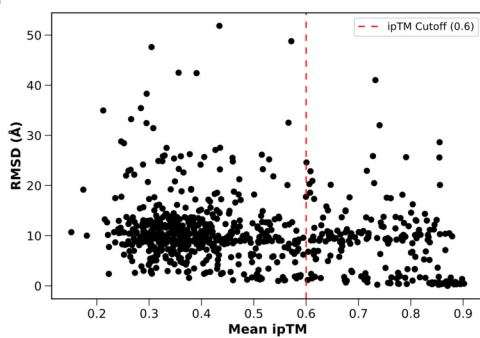
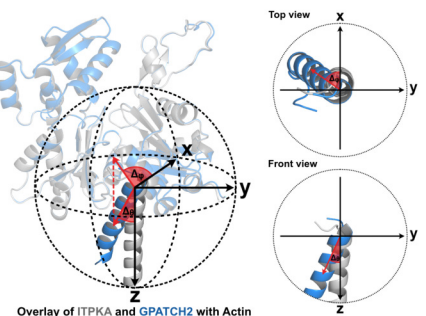
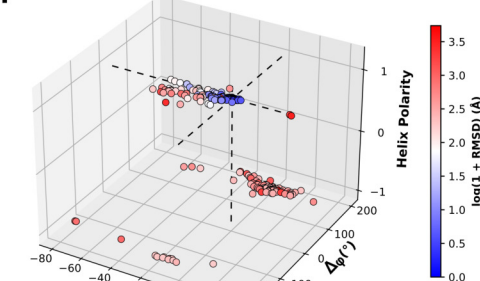
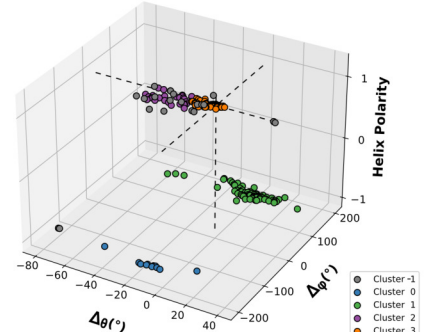
## References

1. Arai, A., Spencer, J. A. & Olson, E. N. STARS, a Striated Muscle Activator of Rho Signaling and Serum Response Factor-dependent Transcription. *Journal of Biological Chemistry* **277**, 24453–24459 (2002).
2. Schulze, J. O. *et al.* Structural and functional characterization of human Iba proteins. *The FEBS Journal* **275**, 4627–4640 (2008).
3. Banerjee, J., Fischer, C. C. & Wedegaertner, P. B. The Amino Acid Motif L/Ilx<sub>x</sub>FE Defines a Novel Actin-Binding Sequence in PDZ-RhoGEF. *Biochemistry* **48**, 8032–8043 (2009).
4. Boeynaems, S. *et al.* Aberrant phase separation is a common killing strategy of positively charged peptides in biology and human disease. Preprint at <https://doi.org/10.1101/2023.03.09.531820> (2023).
5. Zhan, Q. Q., Wong, S. S. & Wang, C. L. A calmodulin-binding peptide of caldesmon. *Journal of Biological Chemistry* **266**, 21810–21814 (1991).
6. D'Atri, F. & Citi, S. Cingulin interacts with F-actin in vitro. *FEBS Letters* **507**, 21–24 (2001).
7. Chrifi, I. *et al.* Cgnl1, an endothelial junction complex protein, regulates GTPase mediated angiogenesis. *Cardiovascular Research* **113**, 1776–1788 (2017).
8. Scherer, A. N., Anand, N. S. & Koleske, A. J. Cortactin stabilization of actin requires actin-binding repeats and linker, is disrupted by specific substitutions, and is independent of nucleotide state. *Journal of Biological Chemistry* **293**, 13022–13032 (2018).
9. Marat, A. L., Ioannou, M. S. & McPherson, P. S. Connecdenn 3/DENND1C binds actin linking Rab35 activation to the actin cytoskeleton. *MBoC* **23**, 163–175 (2012).
10. Wang, X. *et al.* DIXDC1 isoform, I-DIXDC1, is a novel filamentous actin-binding protein. *Biochemical and Biophysical Research Communications* **347**, 22–30 (2006).
11. Zhao, B.-W. *et al.* FBXO34 Regulates the G2/M Transition and Anaphase Entry in Meiotic Oocytes. *Front. Cell Dev. Biol.* **9**, 647103 (2021).
12. Estrada, L. Fgd1, the Cdc42 guanine nucleotide exchange factor responsible for faciogenital dysplasia, is localized to the subcortical actin cytoskeleton and Golgi membrane. *Human Molecular Genetics* **10**, 485–495 (2001).

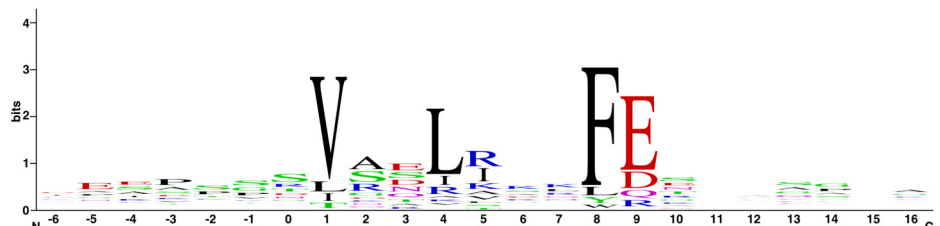
13. Hao, J.-J., Zhu, J., Zhou, K., Smith, N. & Zhan, X. The Coiled-coil Domain Is Required for HS1 to Bind to F-actin and Activate Arp2/3 Complex. *Journal of Biological Chemistry* **280**, 37988–37994 (2005).
14. Johnson, H. W. & Schell, M. J. Neuronal IP<sub>3</sub> 3-Kinase is an F-actin–bundling Protein: Role in Dendritic Targeting and Regulation of Spine Morphology. *MBoC* **20**, 5166–5180 (2009).
15. Brehm, M. A., Schreiber, I., Bertsch, U., Wegner, A. & Mayr, G. W. Identification of the actin-binding domain of Ins(1,4,5) P3 3-kinase isoform B (IP3K-B). *Biochemical Journal* **382**, 353–362 (2004).
16. Inokuchi, J. *et al.* Deregulated expression of KRAP, a novel gene encoding actin-interacting protein, in human colon cancer cells. *J Hum Genet* **49**, 46–52 (2004).
17. Rivera Alvarez, J. *et al.* The kinesin Kif21b regulates radial migration of cortical projection neurons through a non-canonical function on actin cytoskeleton. *Cell Reports* **42**, 112744 (2023).
18. Abé, T. *et al.* Ladinin-1 in actin arcs of oral squamous cell carcinoma is involved in cell migration and epithelial phenotype. *Sci Rep* **14**, 22778 (2024).
19. Maul, R. S. *et al.* EPLIN regulates actin dynamics by cross-linking and stabilizing filaments. *The Journal of Cell Biology* **160**, 399–407 (2003).
20. Wong, M. J., Malapitan, I. A., Sikorski, B. A. & Jongstra, J. A cell-free binding assay maps the LSP1 cytoskeletal binding site to the COOH-terminal 30 amino acids. *Biochimica et Biophysica Acta (BBA) - Molecular Cell Research* **1642**, 17–24 (2003).
21. Cervero, P., Wiesner, C., Bouissou, A., Poincloux, R. & Linder, S. Lymphocyte-specific protein 1 regulates mechanosensory oscillation of podosomes and actin isoform-based actomyosin symmetry breaking. *Nat Commun* **9**, 515 (2018).
22. Sandeep, P. *et al.* Neuron navigators: A novel frontier with physiological and pathological implications. *Molecular and Cellular Neuroscience* **127**, 103905 (2023).
23. Fauchereau, F. The RhoGAP activity of OPHN1, a new F-actin-binding protein, is negatively controlled by its amino-terminal domain. *Molecular and Cellular Neuroscience* **23**, 574–586 (2003).

24. Kelber, J. A. & Klemke, R. L. PEAK1, a Novel Kinase Target in the Fight Against Cancer. *Oncotarget* **1**, 219–223 (2010).
25. Nguyen, T. T. T. *et al.* PLEKHG3 enhances polarized cell migration by activating actin filaments at the cell front. *Proc. Natl. Acad. Sci. U.S.A.* **113**, 10091–10096 (2016).
26. Oliver, C. J. *et al.* Targeting Protein Phosphatase 1 (PP1) to the Actin Cytoskeleton: the Neurabin I/PP1 Complex Regulates Cell Morphology. *Molecular and Cellular Biology* **22**, 4690–4701 (2002).
27. Barnes, A. P., Smith, F. D., VanDongen, H. M., VanDongen, A. M. J. & Milgram, S. L. The identification of a second actin-binding region in spinophilin/neurabin II. *Molecular Brain Research* **124**, 105–113 (2004).
28. Smith, C. *et al.* Septin 9 Exhibits Polymorphic Binding to F-Actin and Inhibits Myosin and Cofilin Activity. *Journal of Molecular Biology* **427**, 3273–3284 (2015).
29. Maas, M. N. *et al.* Examining prestructured  $\beta$ -actin peptides as substrates of histidine methyltransferase SETD3. *Sci Rep* **14**, 26439 (2024).
30. Hildebrand, J. D. & Soriano, P. Shroom, a PDZ Domain–Containing Actin-Binding Protein, Is Required for Neural Tube Morphogenesis in Mice. *Cell* **99**, 485–497 (1999).
31. Yeo, N. C. *et al.* Shroom3 contributes to the maintenance of the glomerular filtration barrier integrity. *Genome Res.* **25**, 57–65 (2015).
32. Fredriksson-Lidman, K., Van Itallie, C. M., Tietgens, A. J. & Anderson, J. M. Sorbin and SH3 domain-containing protein 2 (SORBS2) is a component of the acto-myosin ring at the apical junctional complex in epithelial cells. *PLoS ONE* **12**, e0185448 (2017).
33. Mehta, V. *et al.* SPECC1L binds the myosin phosphatase complex MYPT1/PP1 $\beta$  and can regulate its distribution between microtubules and filamentous actin. *Journal of Biological Chemistry* **299**, 102893 (2023).
34. Niwa, R., Nagata-Ohashi, K., Takeichi, M., Mizuno, K. & Uemura, T. Control of Actin Reorganization by Slingshot, a Family of Phosphatases that Dephosphorylate ADF/Cofilin. *Cell* **108**, 233–246 (2002).
35. Chen, Y. *et al.* F-actin and Myosin II Binding Domains in Supervillin. *Journal of Biological Chemistry* **278**, 46094–46106 (2003).

36. Pestonjamas, K. N., Pope, R. K., Wulfkuhle, J. D. & Luna, E. J. Supervillin (p205): A Novel Membrane-associated, F-Actin-binding Protein in the Villin/Gelsolin Superfamily. *The Journal of Cell Biology* **139**, 1255–1269 (1997).
37. Wulfkuhle, J. D. *et al.* Domain analysis of supervillin, an F-actin bundling plasma membrane protein with functional nuclear localization signals. *Journal of Cell Science* **112**, 2125–2136 (1999).
38. Belardi, B. *et al.* A Weak Link with Actin Organizes Tight Junctions to Control Epithelial Permeability. *Developmental Cell* **54**, 792-804.e7 (2020).
39. Pacholsky, D. *et al.* Xin repeats define a novel actin-binding motif. *Journal of Cell Science* **117**, 5257–5268 (2004).

**a****e****b****f****g****h****i****c****d**

| S. cerevisiae ABP140 (Lifeact) | 1 - M G V A D L I K K F E S I - 13  |
|--------------------------------|-------------------------------------|
| H. sapiens ITPKA (F-tractin)   | 29 - R S V G E L R L L F E A R - 41 |
|                                |                                     |

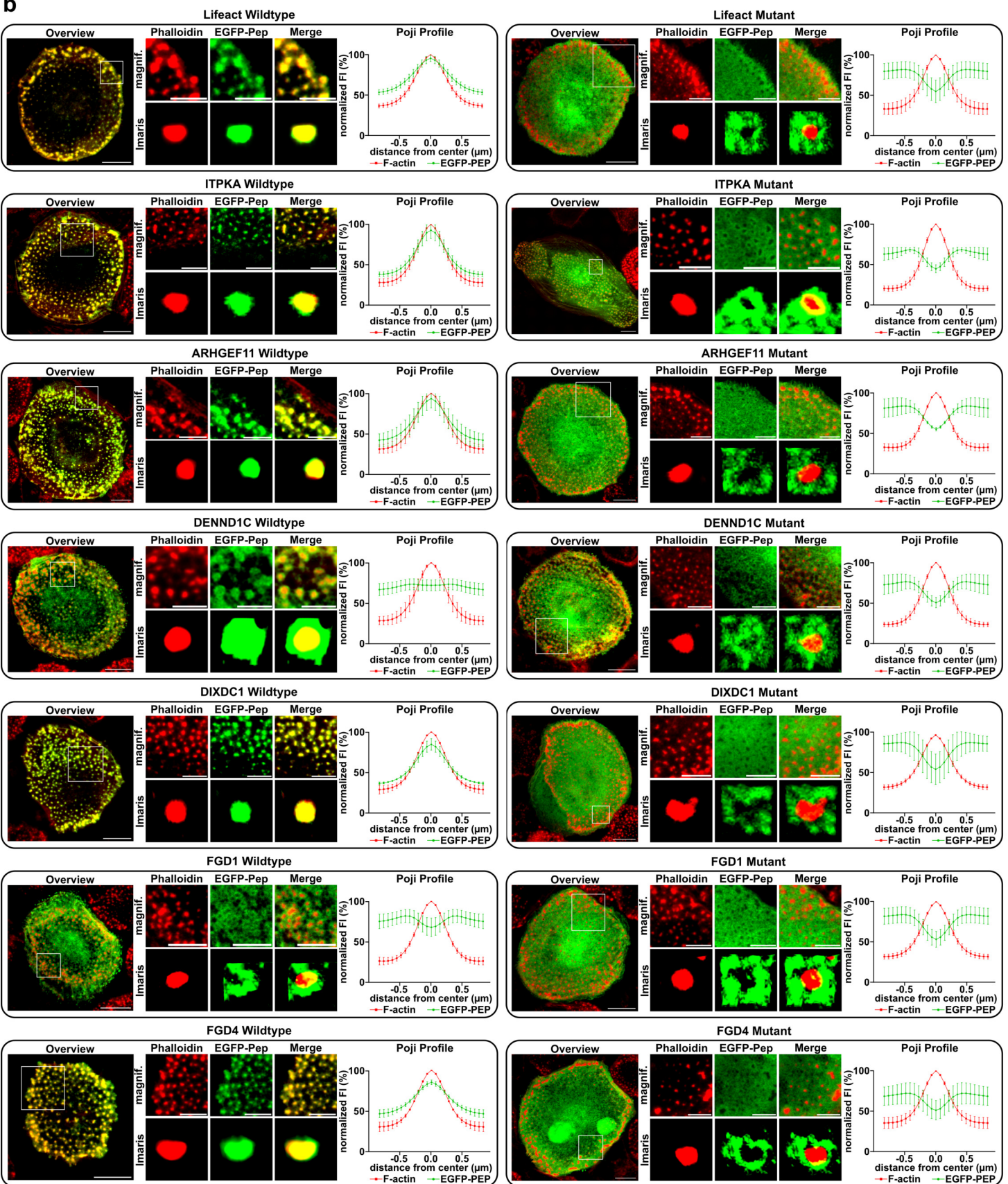
**j**

**a**

**S. cerevisiae ABP140 (Lifeact)**  
**H. sapiens ITPKA (F-tractin)**  
**H. sapiens ARHGEF11**  
**H. sapiens DENND1C**  
**H. sapiens DIXDC1**  
**H. sapiens FGD1**  
**H. sapiens FGD4**

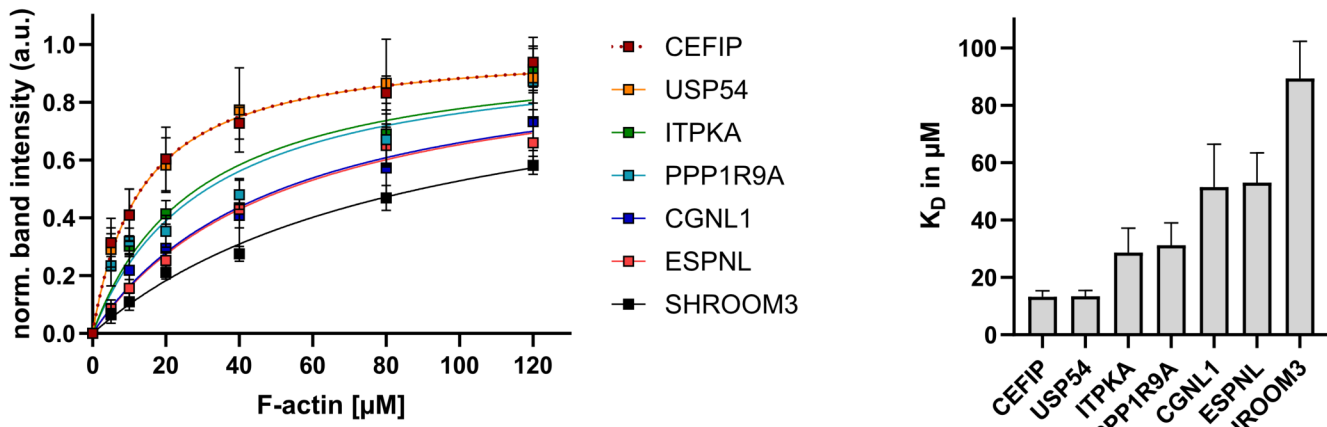
**P1 P4 P8P9**

|   |   |   |   |   |   |   |   |   |   |   |   |   |   |   |   |   |   |   |   |   |   |   |   |
|---|---|---|---|---|---|---|---|---|---|---|---|---|---|---|---|---|---|---|---|---|---|---|---|
| 1 - - - - M G V A D L I K K F E S I S K E E G - 18        |   |   |   |   |   |   |   |   |   |   |   |   |   |   |   |   |   |   |   |   |   |   |   |
| 24 - E R A P R R S V G E L R L L F E A R C A A V A - 46   |   |   |   |   |   |   |   |   |   |   |   |   |   |   |   |   |   |   |   |   |   |   |   |
| 558 - V E V K P G N V R N I I Q H F E N N Q Q Y D A - 580 | V | A | F |   |   |   |   |   |   |   |   |   |   |   |   |   |   |   |   |   |   |   |   |
| 785 - Q P S S R P R V A D L K K C F E G - - - - - 806     | P | R | V | D | K | C | F | E |   |   |   |   |   |   |   |   |   |   |   |   |   |   |   |
| 191 - I E N P Y W S V R A L V Q Q Y E G Q Q R S P S - 213 | I | E | N | P | Y | W | V | R | A | L | V | Q | Y | E | G | Q | Q | R | S | P | S |   |   |
| 201 - A S P S S A A V S S L I E K F E R E P V I V A - 226 | A | S | P | S | S | A | V | S | S | L | I | E | K | F | E | R | E | P | V | I | V | A |   |
| 13 - S K E K P S K V S D L I S R F E G G S S L S N - 35   | S | K | E | K | P | S | K | V | S | D | L | I | S | R | F | E | G | G | S | S | L | S | N |

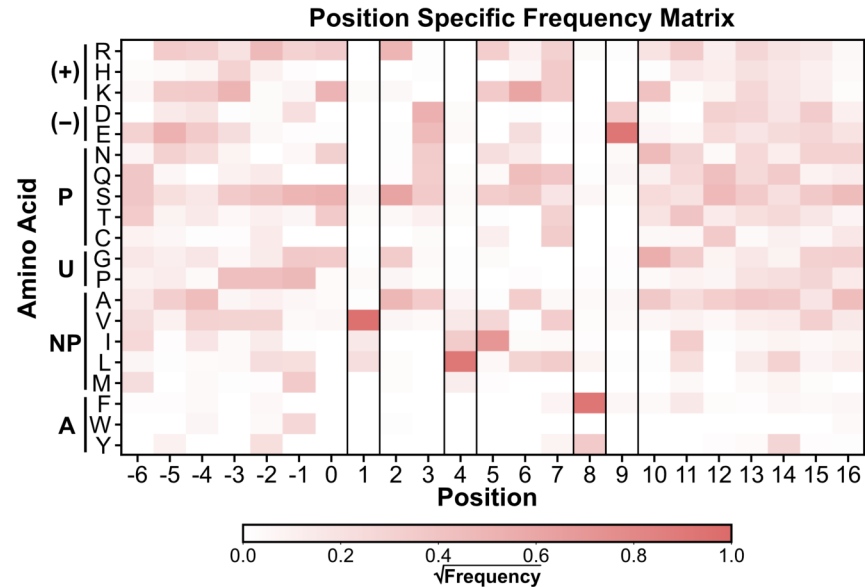
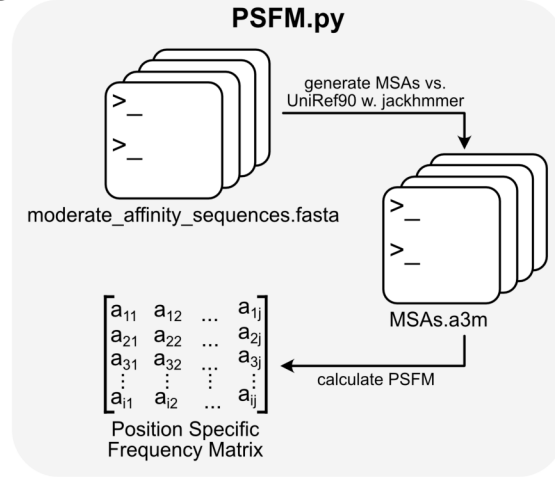
**b**

| S. cerevisiae ABP140 (Lifeact) | 1 - - - - M G V A D L I K K F E S I S K E E G - 18          |
|--------------------------------|---|
| H. sapiens ITPKA (F-tractin)   | 24 - E R A P R R S V G E L R L L F E A R C A A V A - 46     |
| H. sapiens CGNL1               | 346 - D T G S I P G V D Q L I E K F D Q K P G L Q R - 369   |
| H. sapiens CEFIP               | 136 - S N K P V S K V S T L I K S F D R T E S Q R C - 159   |
| H. sapiens ESPNL               | 645 - I Q E W G V S V R T L R G N F E S A S G P L C - 668   |
| H. sapiens PPP1R9A             | 195 - T E A V S P T V S Q L S A V F E N T D S P S A - 218   |
| H. sapiens SHROOM3             | 774 - Y G K P H C S V L E K V S K F E Q R E Q G S Q - 797   |
| H. sapiens USP54               | 1121 - F P S T K G L V R S L A E Q F Q R M Q G V S M - 1144 |

b



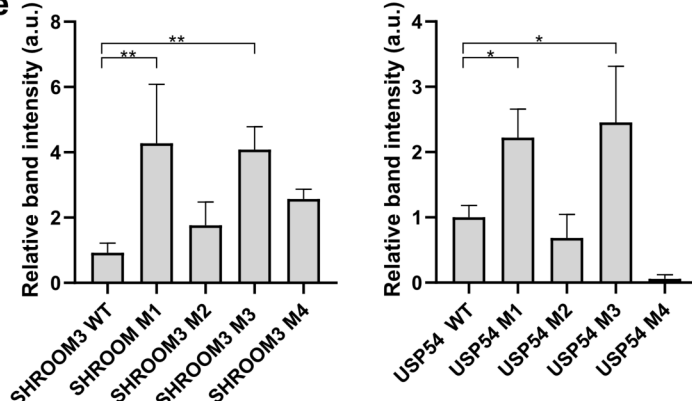
c



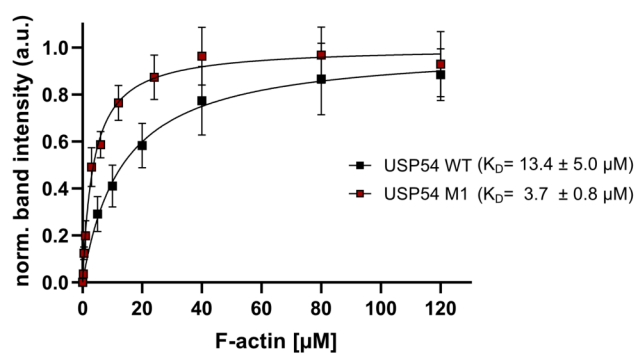
d

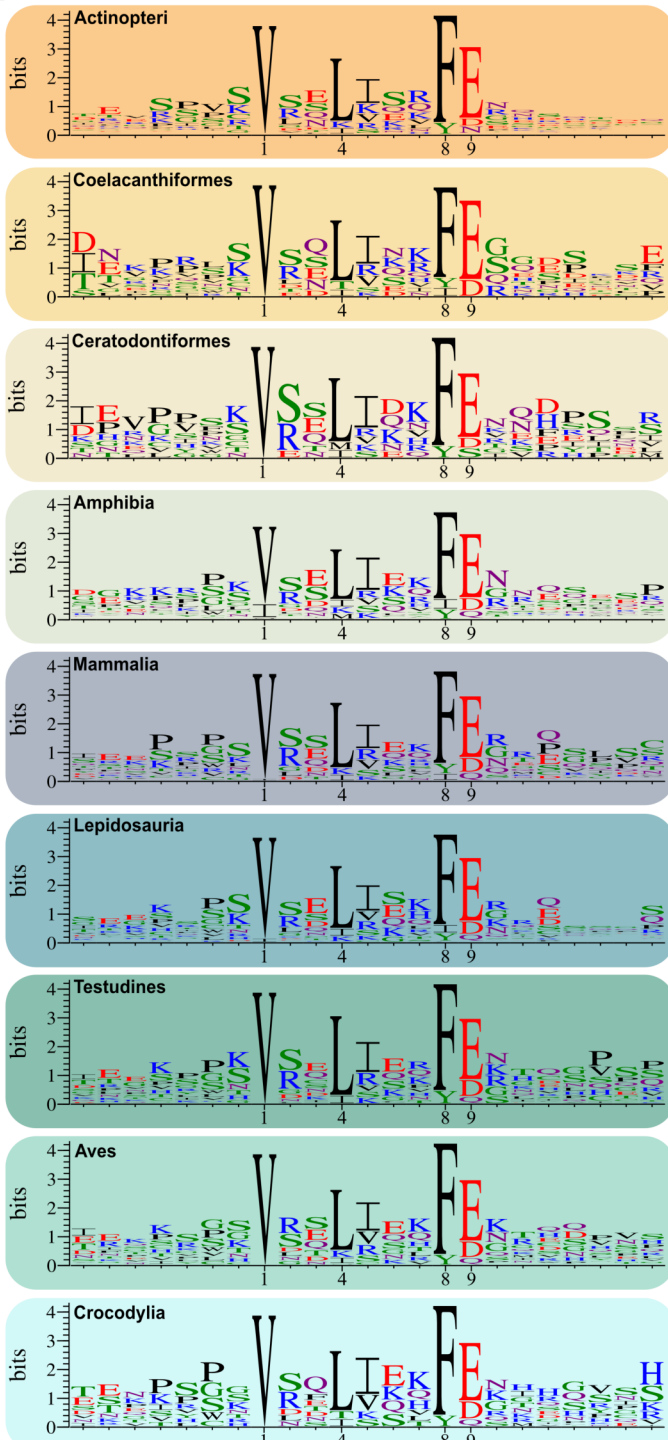
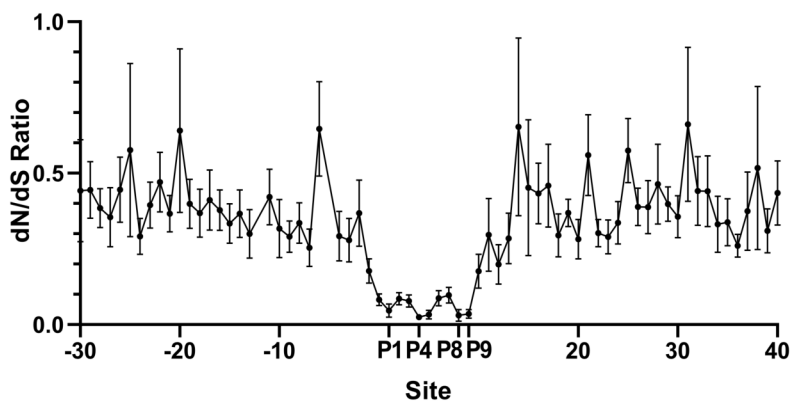
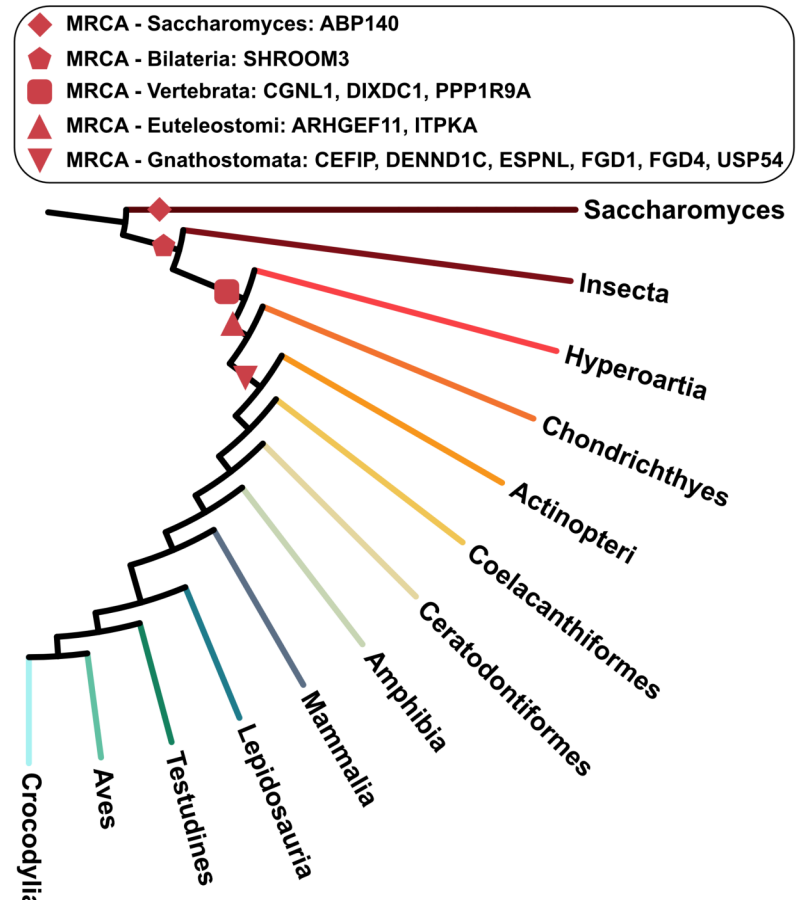
|                       |   | P1 | P4 | P8P9 |                     | P1  | P4 | P8P9 |  |
|-----------------------|---|----|----|------|---------------------|---|----|------|--|
| H. sapiens SHROOM3 WT | Y G K P H C S V L E K V S K F E Q R E Q G S Q   |    |    |      | H. sapiens USP54 WT | F P S T K G L V R S L A E Q F Q R M Q G V S M |    |      |  |
| H. sapiens SHROOM3 M1 | I G K P H S S V L E L V S K F E A R C Q G S A   |    |    |      | H. sapiens USP54 M1 | I P S T K G S V R S L I E Q F E R I Q G V S A |    |      |  |
| H. sapiens SHROOM3 M2 | I G K P H S S V L E K V S K F E A R C Q G S A   |    |    |      | H. sapiens USP54 M2 | I P S T K G S V R S L A E Q F Q R M Q G V S M |    |      |  |
| H. sapiens SHROOM3 M3 | I G K P H S S S V L E L V S K F E A R C Q G S A |    |    |      | H. sapiens USP54 M3 | F P S T K G L V R S L I E Q F E R M Q G V S M |    |      |  |
| H. sapiens SHROOM3 M4 | I G K P H S S S V L E L V S K F E A R C Q G S A |    |    |      | H. sapiens USP54 M4 | F P S T K G L V R S L A E Q F Q R I Q G V S A |    |      |  |

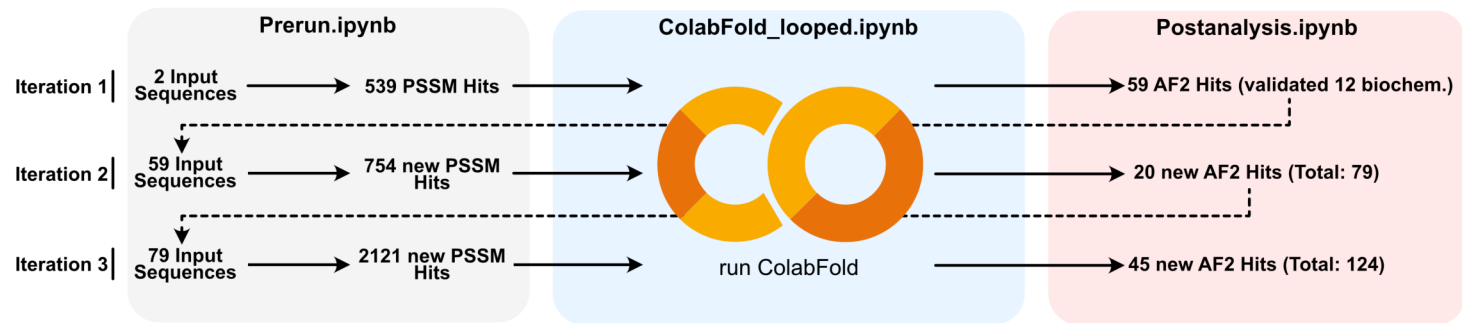
e



f



**a****b****c**

**a****b**